AGU100 ADVANCING EARTH AND SPACE SCIENCE

Geochemistry, Geophysics, Geosystems

RESEARCH ARTICLE
10.1029/2017GC007370

Key Points:
- Knowing the *S* wave speed precisely with a loose constraint on mantle attenuation places strong constraints on the temperature
- The frequency dependence of anelasticity α is variable: ~0.1 in cold/lithospheric mantle and ~0.3 in warm/asthenospheric mantle
- Either partial melting or elastically accommodated grain boundary sliding is required to explain the slowest wave speeds at 130 km

Supporting Information:
- Supporting Information S1

Correspondence to:
L. Cobden,
l.j.cobden@uu.nl

Citation:
Cobden, L., Trampert, J., & Fichtner, A. (2018). Insights on upper mantle melting, rheology, and anelastic behavior from seismic shear wave tomography. *Geochemistry, Geophysics, Geosystems*, *19*, 3892–3916. https://doi.org/10.1029/2017GC007370

Received 19 DEC 2017
Accepted 6 SEP 2018
Accepted article online 1 OCT 2018
Published online 24 OCT 2018

Insights on Upper Mantle Melting, Rheology, and Anelastic Behavior From Seismic Shear Wave Tomography

Laura Cobden[1], **Jeannot Trampert**[1], **and Andreas Fichtner**[1,2]

[1]Department of Earth Sciences, Utrecht University, Utrecht, Netherlands, [2]Department of Earth Sciences, ETH Zurich, Zurich, Switzerland

Abstract In seismic tomography we map the wave speed structure inside the Earth, but we ultimately seek to interpret those images in terms of physical parameters. This is challenging because many parameters can *trade-off* with each other to produce a given wave speed. The problem is compounded by the convention of mapping seismic structures as perturbations relative to a 1-D reference model, rather than absolute wave speeds. Using a full waveform tomography model of Europe as a case study, we quantify the extent to which thermochemical and dynamic properties can be constrained using only *S* wave speed, expressed in absolute values. The wave speed distributions of this tomography model are compared with 4 million thermochemical models, whose seismic properties are computed via thermodynamic modeling. These models sample the full range of realistic mantle compositions, including variable water and melt contents, and mineral intrinsic anelasticity is taken into account. Intrinsic anelasticity causes waves to travel more slowly at higher temperatures, leading to seismic attenuation, but the sensitivity of the wave speed reduction to temperature is, in turn, controlled by the wave frequency. Global studies of surface waves indicate an anticorrelation between *S* wave speed and attenuation. We therefore only retain thermochemical models satisfying this anticorrelation. Our study indicates that the frequency dependence of anelasticity, α, depends on temperature or rheology, with $\alpha \approx 0.1$ being most appropriate in cold or lithospheric mantle and $\alpha \approx 0.3$ in warmer regions (i.e., the asthenosphere). Additionally, the slowest regions require specific compositions and/or a velocity-weakening mechanism, such as partial melting, elastically accommodated grain boundary sliding, or water.

1. Introduction

On a global scale, seismic tomography has provided tantalizing images of the Earth's interior, showing extensive, fast structures—thought to be subducting slabs—in the lower mantle (Van der Hilst et al., 1997), and narrower, slow structures, which have been interpreted as plumes (e.g., French & Romanowicz, 2015; Montelli et al., 2004). While the procedure for mapping 3-D wave speed structure inside the Earth has been established for several decades, it is only recently that computational resources have allowed the application of inversion techniques that exploit the full seismic waveform. This full waveform tomography enables us to map shorter wavelength, high-amplitude wave speed anomalies, that would traditionally be damped and spatially smeared using tomography based on asymptotic techniques (e.g., Rickers et al., 2012). The increasing resolution of tomographic models is an increasing impetus to quantitatively interpret the images in terms of thermochemical structure. Such interpretations may provide important insights into dynamic and tectonic processes that would otherwise go undetected or unconstrained. However, interpretation of seismic wave speed alone is inherently nonunique. Conventionally, seismic tomography maps the lateral variations (perturbations or anomalies) in wave speed from a reference model, rather than absolute values. In classical (linearized) tomography, this works, but the problem for interpretation is that we cannot define a 1-D thermochemical model corresponding to the seismological reference model (Cobden et al., 2008, 2009). Additionally, lateral variations in wave speed can be generated by both thermal and chemical changes, and distinguishing between the two, especially in light of data uncertainties, is challenging (e.g., Deschamps & Trampert, 2003).

In seismology it is common practice to work with perturbations from a 1-D reference model because we know the average (1-D) wave speed structure of the Earth fairly well. This linearizes the problem, but in reality, the seismic data depend very nonlinearly on the wave speed structure. This nonlinearity can be taken into account properly by iterating as in full waveform inversion, which in turn has been shown

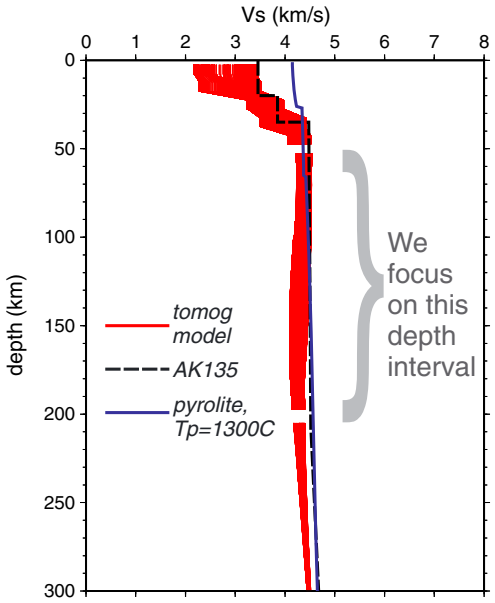

Figure 1. V_S ranges of the tomography model (Fichtner et al., 2013) as a function of depth from 0 to 300 km. AK135 and adiabatic pyrolite (anharmonic V_S) are shown for comparison.

to produce models with much higher-amplitude (lateral) variations in the wave speeds than linear methods (e.g., Trampert & Fichtner, 2013; Zhu et al., 2015). Full waveform imaging thus naturally produces absolute wave speeds, taking into account full nonlinearity and depending much less on regularization and damping. This simplifies the task of a thermochemical interpretation, as no reference state needs to be defined.

When we work with absolute values, we can easily exclude extreme temperatures or compositions that are petrologically or dynamically implausible. We can also, correspondingly, place constraints on the absolute values of mantle temperature or chemistry, rather than only the amplitude of lateral variations from an uncertain thermochemical reference state.

As a case study, we examine the absolute *S* wave speed (V_s) structure beneath Europe, obtained from a full waveform inversion (Fichtner et al., 2013). We focus on the depth interval between 50 and 200 km, spanning the transition from lithospheric to asthenospheric mantle. The *S* wave speeds in this region are in general slower than the global average (Figure 1).

However, one of the most striking features is especially low wave speeds (3.76–4.0 km/s) that occur beneath Iceland and other parts of the mid-Atlantic ridge, as well as beneath Iberia, which reach a minimum wave speed between ~120 and 130 km (Figure 2). Such low velocities have also been observed in other regions, for example, beneath the East Pacific Rise (Yang et al., 2007), the Lau Basin (Wei et al., 2015), and Japan Sea (Simutė et al., 2016). There is currently no consensus on their origin, with both partial melt (Yang et al., 2007) and mineral intrinsic anelasticity (e.g., Goes et al., 2012; Priestley & McKenzie, 2006) having been implicated. Water may enhance or contribute to both these effects. Recently, Karato et al. (2015) proposed an additional mechanism of *elastically accommodated grain boundary sliding* (EA-GBS). EA-GBS is a velocity-weakening mechanism, which may be activated at moderate temperatures (~900 ± 300 K) at middle to deep lithospheric pressures. Below the activation temperature, grain positions (in a polycrystalline aggregate) are essentially fixed. At the activation temperature, the grain boundaries weaken and sliding can take place along the boundaries, leading to elastic deformation of the grains. This reduces the elastic modulus and can hence lead to significant reduction in the wave speed (referred to as velocity weakening).

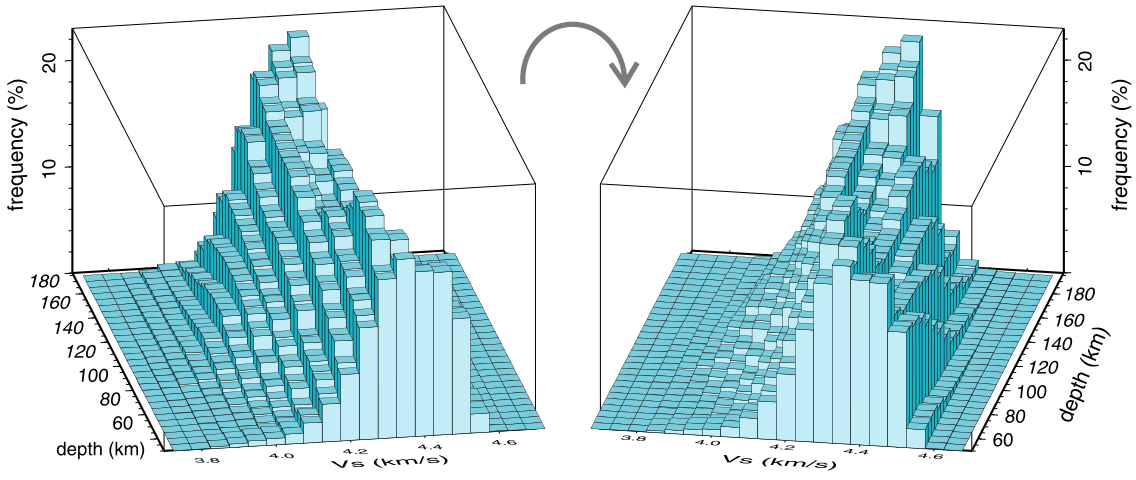

Figure 2. Frequency distributions of the *S* wave speed as a function of depth, for the tomography model of Fichtner et al. (2013). Plot on right is simply a rotated view of the plot on the left. Starting at 52 km, the slowest wave speeds become more abundant with depth, reaching a peak at ~120–140 km.

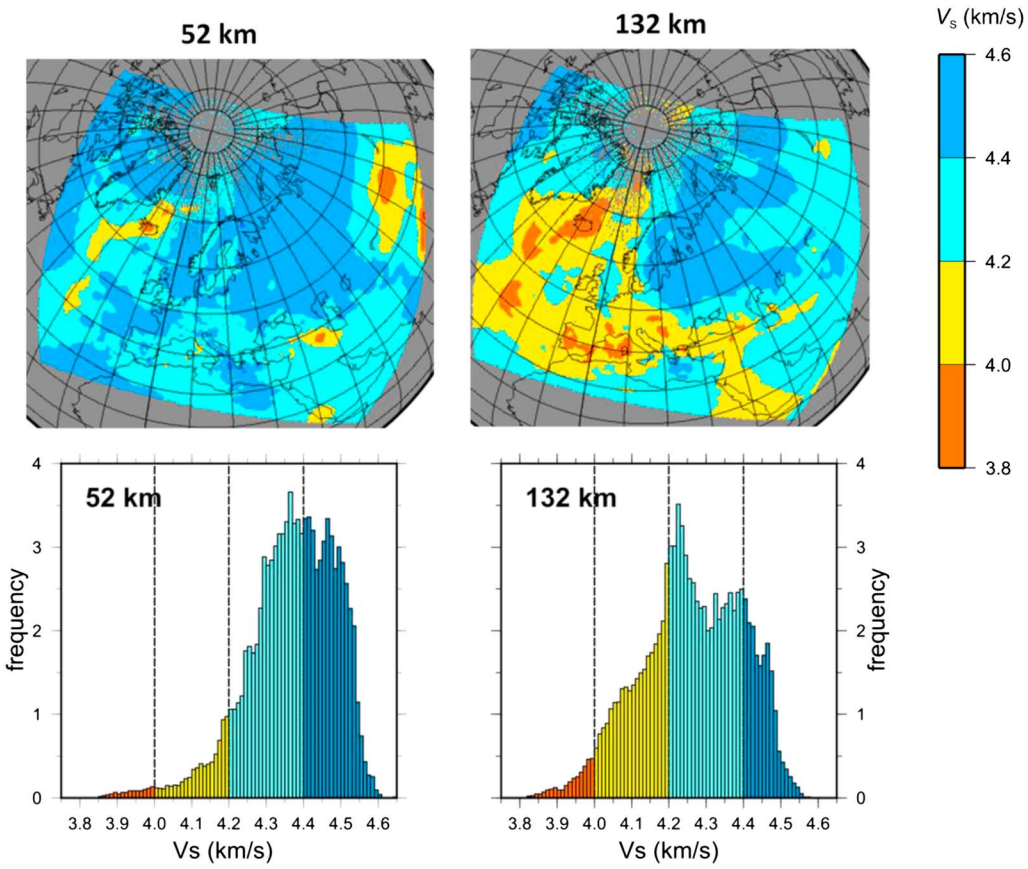

Figure 3. Case study: V_S (top) maps and (bottom) distributions at two representative depths in the tomography model, divided into four *bands* for interpretation purposes. The histograms show the frequency (in percent) with which each V_S value occurs at that depth. The vertical dashed lines represent the division of the full distributions into four bands of width ~0.2 km/s. The orange regions ($V_S < 4.0$ km/s) are especially slow.

We use thermodynamic modeling to predict the seismic wave speeds corresponding to different thermochemical structures, in order to find physical models that quantitatively fit the wave speeds occurring in the tomography model. Because of the trade-off between the various thermal and chemical parameters in producing a given wave speed, we define extremely broad ranges of temperature and composition. We then select millions of models drawn at random from within those ranges, in a Monte Carlo procedure. We want to test whether those broad ranges can be narrowed into something smaller for different regions of the tomography model (and hence provide constraints on the thermochemical structure), given that our only observable is the *S* wave speed.

In the tomography model, V_S is specified every 5 km in depth and every 0.25° in latitude and longitude, giving a total of 3,024,000 grid points (or 100,800 grid points at each depth). This is a very large number of V_S data, and so we use a statistical approach to identify physical processes and trends beneath Europe (rather than seeking deterministic thermochemical models). In particular, at each depth we compile a histogram showing the frequency with which each V_S value occurs, as shown in Figure 2.

At each depth, we arbitrarily divided the tomography model into four regions on the basis of their wave speed: *Very slow* regions are those in which the *S* wave speed (V_S) is less than 4.0 km/s; *slow* regions have $4.0 < V_S < 4.2$ km/s; *fast* regions have $4.2 < V_S < 4.4$ km/s; and *very fast* regions have $V_S > 4.4$ km/s (see Figure 3). In the interests of brevity, in this paper we show a detailed analysis at two representative depths: 52 km (typically the mid-lithosphere) and 132 km (typically the asthenosphere). We are interested in whether different dynamic and tectonic processes can be distinguished for the four regions; ultimately, much of our interpretation is focused on the very slow regions.

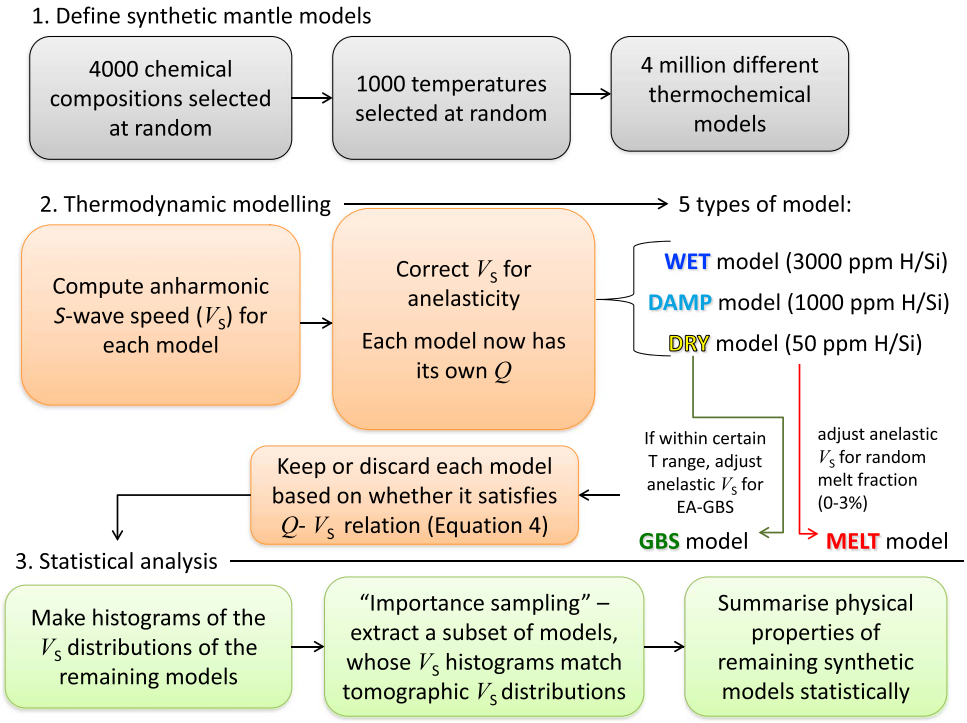

Figure 4. Workflow in this study.

2. Methods

2.1. Philosophy of the Approach

We summarize the workflow for our approach in Figure 4. Details of the thermodynamic modeling for computing the *S* wave speeds of the different thermochemical models, and the motivation behind the ranges of temperature and composition that are modeled in this study (Steps 1 and 2 in Figure 4), are described below. In section 3 we describe the statistical procedure for fitting the thermochemical models to the tomography model (Step 3 in Figure 4).

2.2. Thermodynamic Modeling

We use the thermodynamic modeling code *Perple_X* (Connolly, 1990; Connolly, 2005) to predict the *S* wave speed structure corresponding to a given thermochemical structure. In *Perple_X*, physical properties are computed at regular intervals within a chosen range of pressure (*P*) and temperature (*T*). *Perple_X* performs a Gibbs' free energy minimization to determine the mineral phase relations at each (*P*,*T*) point in the model and computes the bulk elastic properties of the mineral assemblage (including V_S) via an equation of state. In our study, the mineral elastic and solid solution parameters required as input to *Perple_X* are taken from Stixrude and Lithgow-Bertelloni (2011) and we use the equation of state of Stixrude and Lithgow-Bertelloni (2005). Since all input mineral parameters were derived within the same thermodynamic framework, the output phase relations and elastic properties are consistent with each other.

2.3. Selecting the Ranges of Temperature and Chemical Composition

Previous interpretations of seismic tomography have often assumed a fixed chemical composition for the upper mantle, or considered a small selection of common mantle compositions (e.g., Cammarano et al., 2003; Goes et al., 2000). The seismic structure is then interpreted purely in terms of temperature, hydration, and melt. This simplification is based on the observation that, within the range of petrologically plausible compositions, the sensitivity of seismic wave speeds to changes in composition is small compared to the effect of changes in temperature (Goes et al., 2000) and, historically, below the resolution of tomography. However, with the finer resolution afforded by full waveform tomography, compositional changes may be

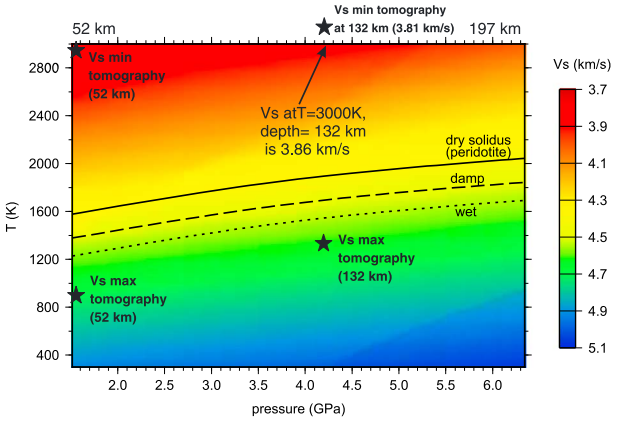

Figure 5. V_S ranges for pyrolitic composition in depth range of study and $300 < T < 3{,}000$ K. Dry, damp, and wet solidi for perodotite are shown for comparison. The solidi are derived from Zerr et al. (1998) and Katz et al. (2003).

visible. Additionally, we found that for Europe, assuming a fixed composition of pyrolite would require the slowest parts of the tomography model to be at temperatures of the order of 3000 K, that is, well above the solidus and completely unrealistic at this depth (Figure 5).

We therefore allowed both the temperature and chemical composition to vary in our analysis, taking wide ranges that should encompass all petrologically feasible options for the upper mantle as well as crustal rocks. Compositional ranges were based on a large compilation of mantle xenoliths (Afonso et al., 2013) and additionally the crustal rocks basalt and granulite (Deschamps et al., 2012; Hieronymus & Goes, 2010). We included crustal compositions because in some regions (e.g., beneath the Himalayas), this may be reasonable, and also to gain a complete picture of the maximum sensitivity of V_s to composition. Temperatures were restricted so as not to exceed the solidus of harzburgite (Maaløe, 2004), which we assume is the most refractory chemical composition of the upper mantle.

Four thousand different chemical compositions were chosen, expressed in terms of weight percent of the six major mantle oxides MgO, SiO_2, FeO, Al_2O_3, CaO, and Na_2O (NCFMAS system), and following the distributions shown in Figure 6. It is impossible to generate six uniform distributions when the maximum and minimum allowed weight percent (as defined by petrological constraints) are different for each oxide, and the total percent must equal 100. Therefore, first we drew 4,000 random models in which the maximum and minimum allowed weight percent of each oxide were set a few percent beyond the ranges observed in petrology. This created six uniform distributions, but for each model the total weight percent of the six oxides did not sum to 100. We then normalized the composition to express the relative proportions of each oxide as an actual percentage (i.e., the proportions of the six oxides were kept fixed, while the total weight percent summed to 100%), leading to the distributions in Figure 6. These distributions have maxima corresponding well with the most abundant values seen in mantle xenoliths while the ranges from minimum to maximum cover the full variability of both mantle xenoliths and the major crustal rocks (e.g., see Afonso et al., 2013).

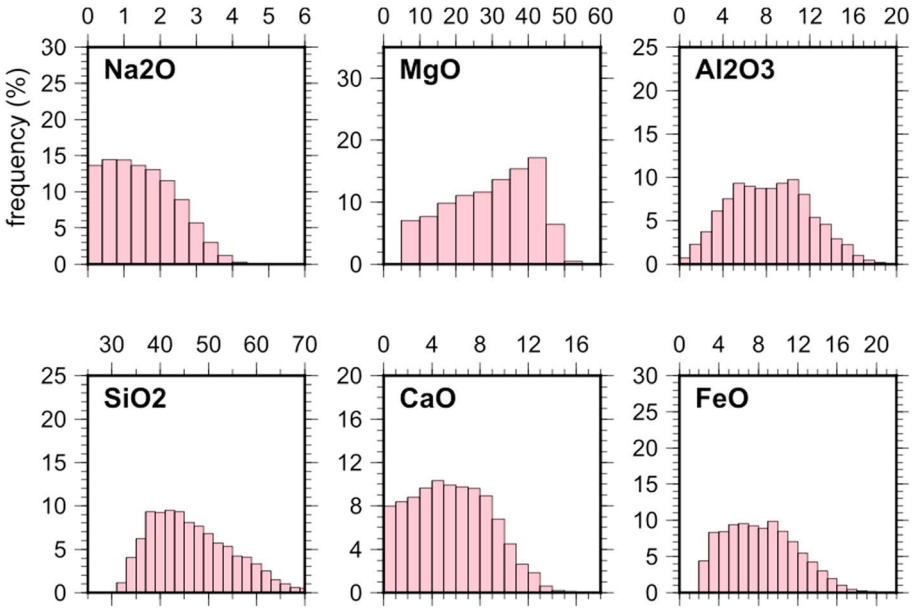

Figure 6. Histograms showing the distributions of each oxide for the 4,000 different chemical compositions modeled in this study. Oxide proportions are in weight %. The peaks of each distribution broadly correspond to the most abundant composition in xenoliths (e.g., Afonso et al., 2013).

At each depth node in the tomography model (which in our case was every 5 km), and for each of the 4,000 chemical compositions, we then picked 1,000 temperatures at random from a uniform distribution. The minimum temperature in the distribution was set to 300 K at all depths. This is of course colder than we would expect in the mantle, but we wanted to see what minimum temperature would come directly from the seismic observations without any imposed (and generally unknown) a priori restriction that might bias the result, and without forcing a sharp boundary in the minimum temperature. (In general we used large ranges for all the thermochemical parameters because we do not want our results to be biased by already putting the answer in at the beginning.) Ideally, we would have liked to set the maximum temperature at the solidus of the given composition, so that we were not calculating velocities of solid material beyond its melting point. However, the solidus varies nonlinearly as a function of chemical composition, and experimentally has only been determined at low pressures and for a limited range of compositions, parameterized differently than the "NCFMAS" format which we input to *Perple_X*. This makes it not straightforward to extrapolate from available experimental data to infer the solidus of each of our 4,000 compositions.

We therefore implemented a loose constraint on the maximum temperature as follows: We assumed that harzburgite is the most refractory chemical composition possible in the upper mantle. The solidus of harzburgite has been observed and parameterized as a function of depth by Maaløe (2004; equation (1)). Following Maaløe (2004), the maximum temperature at each depth is then given by

$$T_{\max} = 1653 + 82.9P \tag{1}$$

where $T_{\max}$ is the maximum temperature in kelvin and P is the pressure in gigapascal.

This provided 4 million different thermochemical models at each depth of the tomography model.

2.4. Velocity-Weakening Mechanisms

By a simple inspection of the maximum and minimum wave speeds in the tomography model, we found that with increasing depth the 4 million thermochemical models all become too fast to fit the very slow regions of the tomography model (i.e., the orange regions in Figure 3. See Figure S0 in the supporting information for the inability of the 4 million models to explain the slowest wave speeds). Some additional form of velocity-weakening mechanism is required to explain these regions, and we considered four possible mechanisms: (1) intrinsic anelasticity, (2) water, (3) melting, and (4) EA-GBS.

2.4.1. Intrinsic Anelasticity

Intrinsic anelasticity is the dissipation of seismic energy as it propagates through a rock and is controlled by the thermal and structural properties of the constituent grains (Karato & Spetzler, 1990). It contributes to attenuation of the seismic signal, although attenuation is also influenced by geometric spreading and scattering. It is believed that seismic attenuation is frequency dependent, following an *absorption band* model (Anderson & Given, 1982). At frequencies within the absorption band, attenuation can be expressed as

$$Q \propto \omega^{\alpha}$$

where Q = 1/attenuation, also known as the quality factor, is the inverse of the fractional loss of energy per wave cycle, ω is the seismic frequency, and α is a dimensionless exponent. The precise value of α—which may be inferred from laboratory experiments, thermodynamic theory, or seismic observations—is very uncertain. Most studies place it in the range 0.1–0.4 (Romanowicz & Mitchell, 2007), although a recent seismic study has indicated that α is itself frequency dependent and may even become negative at long periods (Lekić et al., 2009).

Mineral physics experiments that determine elastic properties are performed at very high frequencies, above the absorption band of seismic attenuation. Under these conditions, the wave speeds are *unrelaxed* and are not significantly weakened by anelasticity. However, the tomography model that we used was derived with a numerical absorption band whose minimum frequency was about 0.01 Hz (i.e., 100-s period) and the model is expressed in its relaxed state. The wave speeds in the tomography model are thus weakened by anelasticity, and in order to compare them with wave speeds of our thermochemical models, which are based on mineral experiments, the latter must be adjusted. We adjusted them to the minimum frequency of the numerical absorption band, that is, 0.01 Hz, which is close enough to the relaxed state. (Note that the seismic data

that were used to construct the tomography model contained a range of frequencies, 8–150 s, but that the tomography model itself gives the wave speed structure evaluated at 100 s).

We follow the procedure of Behn et al. (2009) to calculate anelastic wave speeds (see Appendix A1.). In this standard formalism, Q depends not only on the seismic frequency but also on the temperature and water content (and to a lesser extent, the grain size). The temperature dependence takes an exponential form:

$$Q \propto \exp\left(\frac{\alpha(E + \mathrm{PV})}{\mathrm{RT}}\right) \tag{2}$$

where T is the temperature, E is the activation energy, P is pressure, V is the activation volume, and R is the gas constant. This correction of the wave speeds for anelasticity implicitly associates a Q value with each thermochemical model.

The parameter values that we initially input to the anelasticity equations (given in Appendix A1) are taken from Behn et al. (2009) and are based on experimental observations of polycrystalline olivine (Faul & Jackson, 2005; Jackson et al., 2002; Tan et al., 2001). We refer to this anelasticity correction as "QBehn." We chose this approach rather than a parameterization based on homologous temperatures (e.g., Cammarano et al., 2003) because the homologous temperature cannot be measured directly, whereas the parameters in QBehn are taken directly from experimental observations. Additionally, previous studies have noted that these (standard) parameters and equations, combined with a half-space cooling model, produce wave speeds that are compatible with seismic observations and predict mantle temperatures that are consistent with surface heat flow (Goes et al., 2012, 2000). However, these studies did not impose a constraint on Q, and the slowest regions of these models are associated with Q values $\leq$20. It is difficult to reconcile such low Q with surface wave observations and over resolution lengths of tomographic models. In a regional study of the East Pacific Rise (Yang et al., 2007), surface wave measurements required $Q > 79$ between 55 and 120 km (this is slightly higher than most 1-D reference models at this depth, although comparable within the estimated uncertainties on the 1-D models; Resovsky et al., 2005). In order to reconcile this with their observations of V_s, while having temperatures compatible with a half-space cooling model, the authors reduced the values of α and E (equation (2)) in the anelasticity correction. This adjustment reduces the temperature dependence of anelasticity, while enhancing the effect of a given attenuation on the wave speed. Following Yang et al. (2007), we made a similar modification to our anelasticity correction, reducing α from 0.27 to 0.1, and E from 505 to 255 kJ/mol. We refer to this second anelasticity correction as "QYang." In all subsequent calculations (i.e., water, melting, and grain-boundary sliding), we ran two simulations: one with the QBehn anelasticity correction and one with the QYang correction.

2.4.2. Water

Olivine is the major upper mantle mineral, and although it is nominally anhydrous, it can incorporate a small amount of hydrogen atoms as impurities. For very small degrees of hydration ($\leq$~0.1 wt % H_2O), this has a negligible effect on its elastic properties but reduces the wave speeds through enhancement of anelasticity (Shito et al., 2006). To examine this effect in detail, we ran three sets of anelasticity corrections to the thermochemical models: One for a *dry* mantle (C_{OH} = 50H/10^{6}Si, which is essentially no water), one for a *damp* mantle (1,000H/10^{6}Si), and one for a *wet* mantle (3,000H/10^{6}Si). The variable water content is implemented as a parameter in the anelasticity correction (see Appendix A1.). This produced three sets of 4 million models (dry, wet, and damp), where each set had a different water content, and hence different Q and V_s values, for a given temperature and composition.

2.4.3. Melt

Partial melt is often suggested as a cause of low wave speeds in the shallow mantle (e.g., Anderson & Sammis, 1970), but quantitative and robust identification thereof has been lacking. We therefore sought to test if melting could explain the slow wave speeds in our tomography model. From the dry models, we further generated a set of 4 million melt models, in which a random melt fraction between 0% and 3% was assigned to each model. We adjusted the wave speeds for melt on the basis of numerical modeling experiments (Hammond & Humphreys, 2000a, 2000b) that define the reduction in wave speed as a function of melt fraction and melt geometry. In this framework the melt-solid system is purely mechanical and the melt fraction is independent of the temperature and chemical composition.

Both numerical modeling and seismic observations indicate that the relaxation times of attenuation mechanisms associated with melting (namely, viscous shear relaxation and melt squirt) are too fast to occur in the seismic frequency band (Hammond & Humphreys, 2000a; Karato & Spetzler, 1990). Thus, corrections to the wave speed due to melt should be for the relaxed modulus. The magnitude of the wave speed reduction, in turn, depends nonlinearly on the melt fraction and the geometry of the melt inclusions between solid grains, investigated in detail by Hammond and Humphries (2000b). We assumed a fixed derivative for the melt sensitivity, $\frac{dV_s}{dm}$ = 7.9% per 1% melt (m), which is the relaxed derivative of Hammond and Humphries (2000b) for realistic melt geometry, and corrected our V_s values as follows:

$$Vs_{\text{melt}} = Vs_{\text{anel}} - F\frac{dV_s}{dm}\cdot\frac{Vs_{\text{anel}}}{100} \tag{3}$$

where F is the melt percentage. Depending on the melt geometry, the fixed derivative may slightly overestimate the sensitivity at melt fractions less than 1%, and underestimate it at higher melt fractions, although this value likely corresponds to the most realistic melt geometry. Each thermochemical model is assigned a random melt fraction between 0% and 3%. We did not allow melt fractions above 3%, since equation (3) only applies for smaller melt fractions, and in any case, higher fractions would reduce the wave speeds of all the thermochemical models to less than the slowest values occurring in the tomography model.

2.4.4. Elastically Accommodated Grain-Boundary Sliding

Karato (2014) has suggested, on the basis of petrological and geodynamic observations, that beyond shallow mid-ocean ridges, extensive partial melting in the upper mantle is unlikely, with melt fractions not exceeding ~0.1%. The low velocities observed in the mid to deep lithosphere may thus, alternatively, be explained by EA-GBS (Karato, 2012; Karato et al., 2015). The EA-GBS model presented in Karato et al. (2015) is based on their interpretation of the experimental data published in Jackson and Faul (2010). Depending on the temperature, pressure (i.e., depth), grain size, and water content, EA-GBS has a characteristic seismic frequency at which it becomes activated. We followed the equations given in Karato et al. (2015) to calculate what this frequency would be for each of our "dry" thermochemical models (see Appendix A2.). While our tomography model was derived at a reference frequency of 0.01 Hz, the original seismic data that were used to build the model contained a range of frequencies, up to 0.125 Hz (i.e., 8-s period). Therefore, we only retained dry models for which the characteristic frequency for EA-GBS was between 0.01 and 0.125 Hz. EA-GBS is also thermally activated, and hence at a given depth, will only occur for a finite range of temperatures. We used Figure 3 of Karato et al. (2015) to define these ranges and furthermore only retained models whose temperatures fell within those ranges. This meant that at 52 km, we retained models with temperatures between 900 and 1120 K, and at 132 km, we retained models with temperatures between 1080 and 1300 K. Finally, we used the equations given in Karato et al. (2015) to correct the wave speeds of the remaining models for EA-GBS (see Appendix A2.).

3. Fitting the Synthetic Models to Seismic Observations

3.1. Velocity-Attenuation Constraint

Ideally, any physical interpretation of tomography should satisfy both V_s and Q constraints (Karato, 1993). However, our tomography model only gives a constraint on V_s. It is challenging to measure attenuation from seismograms because it is mostly expressed in the amplitude of seismic waveforms, which are influenced by multiple parameters (Romanowicz, 1994). Additionally, even where Q has been inferred seismically, it is generally unknown to what extent this is due to intrinsic anelasticity, as opposed to scattering or focusing effects (e.g., Trampert & Fichtner, 2013).

During the tomographic inversion of Fichtner et al. (2013), the S wave speed structure was updated at each iteration, while Q was kept fixed and equal to the radially symmetric reference model, QL6 (Durek & Ekström, 1996). While the actual Q structure beneath Europe probably deviates from QL6 and is three-dimensional, the seismograms were fully reconstructed by varying V_s and adjusting the seismic sources, including fitting the amplitudes of the waveforms. This means that the seismic signal corresponding to 3-D Q structure was incorporated into the assumed earthquake source parameters or V_s structure. We therefore consider that Q beneath Europe is essentially unconstrained by this particular tomographic inversion and refer to a global 3-D Q model derived from surface wave observations (Dalton et al., 2009) to place broad constraints on

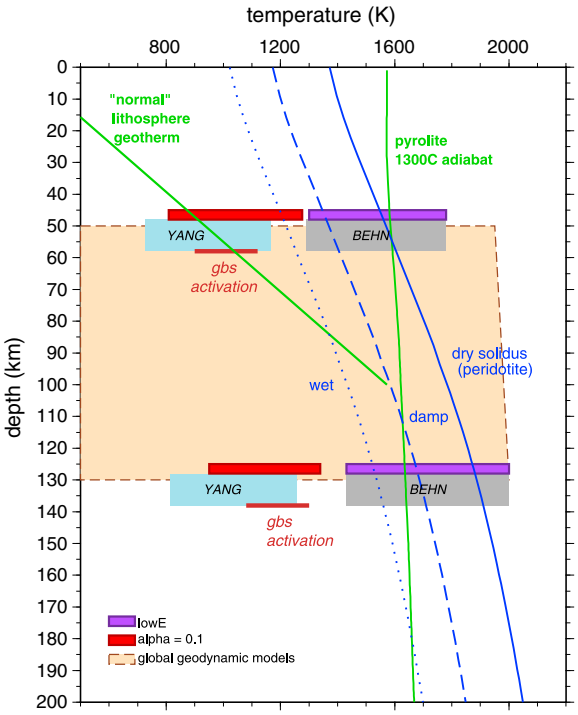

Figure 7. Temperature-depth relations. Gray bands: T ranges of thermochemical models that fit the entire V_s range of the tomography model, using the anelasticity parameters of Behn et al. (2009), at 52 and 132 km. $\alpha = 0.27$, $E = 505$ kJ/mol, and grain size $d = 10$ mm (i.e., QBehn models). Blue bands: T ranges of the thermochemical models for $\alpha = 0.1$ and $E = 255$ kJ/mol ($d = 10$ mm), following Yang et al. (2007; i.e., QYang models). Red bands: Effect of reducing only α to 0.1, relative to QBehn. Purple bands: Effect of reducing only E to 255 kJ/mol. Orange box: Range of temperatures seen in global geodynamic models (Davies et al., 2012). Note that the coldest temperatures of the geodynamic models (~350 K) extend beyond the ranges of this plot. Green lines: 1573 K (i.e., 1300 °C) adiabat for pyrolite and a typical lithospheric (conductive) geotherm. The adiabat is computed from the path of constant entropy for a pyrolitic composition, using thermodynamic modeling code *Perple_X* (Connolly, 2005). Blue lines: Peridotite solidus for dry mantle (solid line), damp mantle (dashed line), and wet mantle (dotted line), based on Zerr et al. (1998) and Katz et al. (2003). Brown bars: Activation temperature for EA-GBS at 52- and 132-km depth, for a seismic frequency of 0.01 Hz.

what the 3-D Q ranges might be. Following Figures 3 and 4 in Dalton et al. (2009), we assumed that the anticorrelation between attenuation and S wave speed can be represented with the following linear relationship:

$$Q^{-1} = 0.152 - 0.031V_s \pm 0.0065 \quad (4)$$

Only thermochemical models whose Q and V_s values were consistent with equation (4) were retained for the next part of the analysis (section 3.2). Essentially, for a given model's V_s value, we only retained it if its corresponding value of Q^{-1} was greater than $(0.152 - 0.031V_s - 0.0065)$ and less than $(0.152 - 0.031V_s + 0.0065)$. This broad constraint captures most of the data points in Figure 4 of Dalton et al. (2009) that in turn represent many different tectonic regions. We preferred this over using an experimentally derived correlation between V_s and Q (Faul & Jackson, 2005) that may only be applicable to certain tectonic regions (Dalton & Faul, 2010) because our tomography model spans different tectonic regimes.

Imposing this constraint places a major restriction on the thermochemical models (see Figures 7 and 8, as well as Figures S7 and S8), with ~1.3–2.3 million models fitting equation (4) in the dry, damp, and wet mantle simulations, and ~150,000–700,000 remaining models in the melt and EA-GBS simulations.

3.2. Reconstructing Seismic Observations From the Synthetic Models

A single observation of V_s cannot be converted into a unique temperature and composition, even using the constraint on Q from equation (4). This is because of the multiple trade-offs between thermochemical parameters in producing a given wave speed. At a fixed temperature and pressure, our range of chemical compositions can generate changes in the S wave speed of up to ~10–12%, that is, similar to the range of wave speed variations seen in full waveform tomography at the same depths (Fichtner et al., 2013; Zhu et al., 2015). When the models are restricted to have a Q-V_s relation satisfying equation (4), compositional variations at a fixed T can still cause V_s variations of up to 5%. This is comparable with the magnitude of wave speed variations in classical tomography. Adding temperature variations will allow even larger changes V_s, or more thermochemical possibilities to produce a fixed V_s. At the same time, uncertainties on the tomography model are not easily defined. For this reason, we do not aim to convert the tomography model into deterministic maps of temperature and composition. Instead, we made histograms of the frequency distributions of V_s at each depth and divided these histograms into four bands of approximately equal width, 0.2 km/s (see Figure 3). Each band is associated with certain geographic areas (Figure 3). We then sought to find thermochemical models whose seismic properties could reproduce these histograms. The reason for fitting the shape of the distributions (and not just the ranges) is that it helps us to assess the relative importance of different thermochemical properties in contributing to the seismic properties. The choice of four bands is somewhat arbitrary: We could have divided the model into narrower or wider bands for a more or less refined interpretation; we chose to study ranges of 0.2 km/s because this seemed sufficient to distinguish and interpret the main features of the tomography model, while allowing for small deviations in the observed and modeled wave speeds due to data uncertainties.

3.2.1. Importance Sampling

We used the Metropolis-Hastings algorithm to determine which thermochemical models can reconstruct the V_s histograms of the tomography model. The Metropolis-Hastings algorithm is a Markov-chain Monte Carlo method, in which one distribution can be reconstructed by drawing samples from another distribution (Mosegaard & Tarantola, 1995). Previously, it has been both efficient and effective for

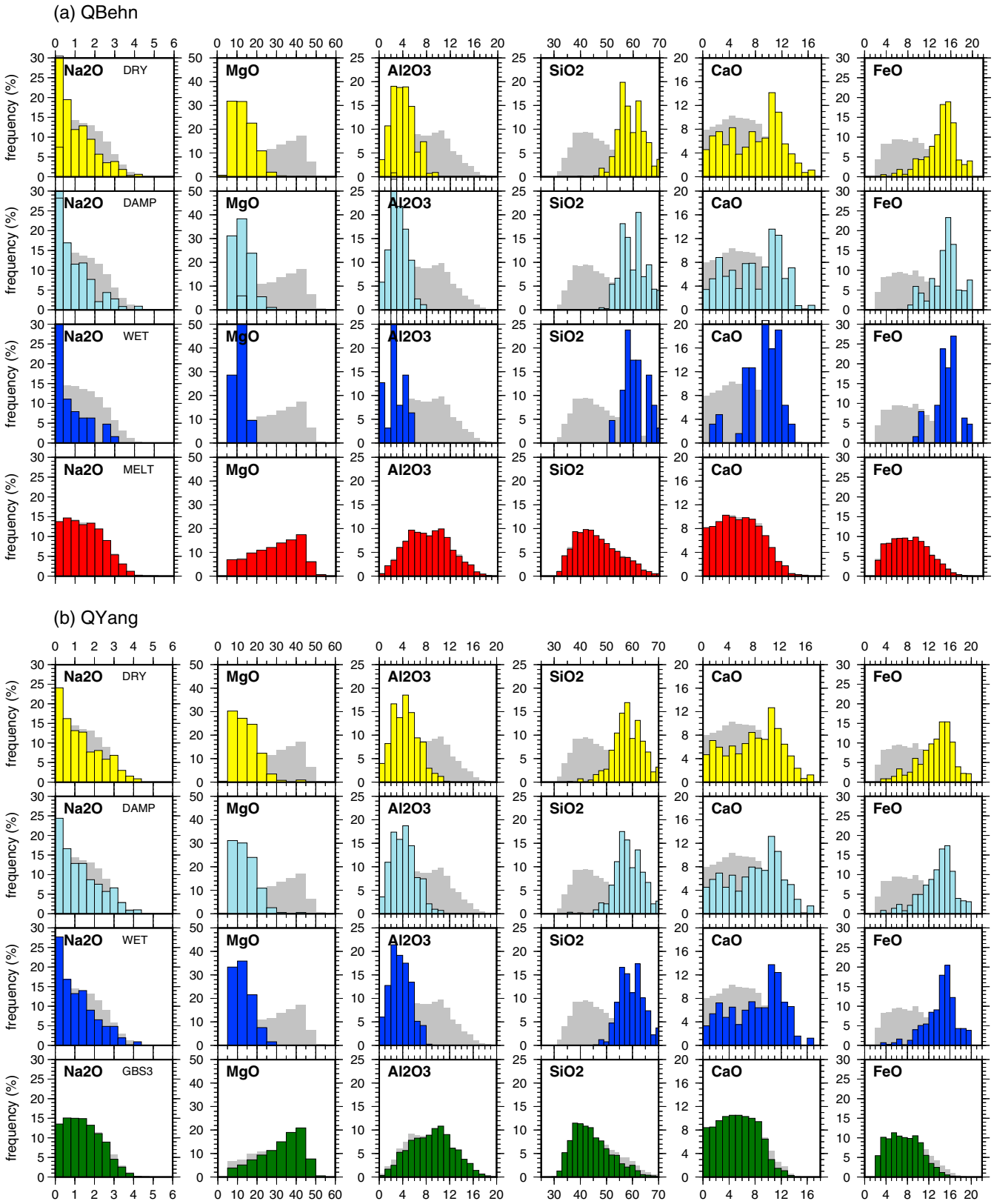

Figure 8. Histograms (frequency distributions) of the chemical compositions, for $V_S < 4.0$ km/s at 132-km depth, expressed as wt % oxides. The gray histograms show the prior distributions, and the colored histograms are the remaining, "best fitting" models after the Metropolis-Hastings algorithm. Models for (a) QBehn and (b) QYang.

thermochemical interpretation of deep mantle structures (Cobden et al., 2012; Mosca et al., 2012). In the first step, the algorithm is shown the two distributions. In our case these distributions would be (A) the V_s histogram of the tomography model at a fixed depth and (B) the V_s histogram of all the thermochemical models at the same depth. The algorithm then reads the V_s of each individual model, which was used to construct the histogram (B), and decides to keep or reject that sample, based on the Metropolis rule applied to the normalized histograms (A) and (B) (see Mosegaard & Tarantola, 1995, for more details). This procedure is referred to as importance sampling. After analyzing all the thermochemical models, a subset of the original models in distribution (B) will have been retained, and a new histogram of the V_s values is constructed (C) from the retained models. If there was a good overlap between (A) and (B) initially, then the new histogram (C) will more closely resemble (A) than (B). If the convergence is not satisfactory, this procedure can then be repeated, until a set of models is obtained that provides the closest possible match to histogram (A). If there is a poor initial overlap between (A) and (B) in the first iteration, only a poor fit to histogram (A) is achieved in the subset of retained models.

4. Results and Interpretation

We tested the fit of five sets of synthetic mantle models: dry, damp, wet, partial melting, and EA-GBS (each with variable temperature and composition), to the V_s distributions of the tomography model, divided into four ranges, at 52 and 132 km, and for two different anelasticity corrections (QBehn and QYang). It is possible that combinations of the five types of model will fit the data, but we were interested in the extent to which each type of mantle model fits, or is required, by the data, individually. In Table 1 we summarize which sets of synthetic model can fit each range of V_s, and in the cases where they do not fit, a short explanation is included. Sometimes the synthetic models simply do not fit the V_s distributions; in other cases there are no models left after imposing the anticorrelation between Q and V_s (equation (4)), and in other cases, the models can be excluded because their temperatures or chemical composition are unfeasible.

The distributions of temperature and chemical composition of the "best fitting" thermochemical models (i.e., those remaining after applying the Metropolis-Hastings algorithm) can be found in Figures S1–S4. These figures also show the corresponding Q distributions of these best fitting models, and the overlap of the V_s distributions of these models, with the tomography model. In general, the degree of overlap between the best fitting models and the tomography model is very high (>99.8%); occasionally, we only achieved a poorer overall fit.

Elastically accommodated grain boundary sliding produces such large wave speed reductions that it is only a viable mechanism when $V_s < \sim$4.0 km/s. In this case, the temperatures of the "best fitting" QBehn models are too high (>1750 K) relative to the moderate temperatures at which EA-GBS is expected to occur (~900–1100 K at 52 km and 1100–1300 K at 132 km, following Karato et al., 2015). Therefore, in the interest of clarity, we did not include these models in any figures, since they are unrealistically hot. Likewise, the temperatures of the best fitting QYang models are very cold relative to the temperatures at which existence of partial melt is feasible, and so melt-bearing models with QYang correction are not plotted. The temperatures of the best fitting melt models with QBehn correction are compatible with partial melting, and so these models are included in the figures.

There are two main consequences of placing a (loose) constraint on the relation between Q and V_s (equation (4)): The first is that in some cases certain sets of models can no longer fit the data (namely, dry models and partial-melt models at 52 km with QBehn correction; see Figures S5 and S6). Second, we acquire a major restriction on the mantle temperature: Within the ranges of V_s of the tomography model (red boxes, Figures S7 and S8), and for those models satisfying equation (4), small differences in temperature correspond to large differences in V_s (see sharp gradient of the colored data points, Figures S7 and S8). This means that each of the four bands into which we divided the V_s distribution of the tomography model corresponds to a very narrow range of model temperatures (see Figures S1–S4), although the absolute temperatures depend on the anelasticity parameters (i.e., QBehn vs. QYang give very different temperature models).

We compared the temperature ranges of the best fitting synthetic models with several reference temperature profiles: (1) a 1300 °C (potential temperature) adiabat for pyrolitic composition; (2) a continental

Table 1
Summary of Which Thermochemical Models Fit Which Sets of Seismic Data

		< 4.0 km/s	4.0-4.2 km/s	4.2-4.4 km/s	> 4.4 km/s
52 km		very slow	slow	fast	very fast
QBEHN	*dry*	× (fails Q-Vs constraint)	✓ (only if hot)	✓ (only if hot)	✓ (only if hot)
	damp	✓ (only if hot, & restricted compositions)	✓ (only if hot)	✓ (only if hot)	✓ (only if hot)
	wet	✓ (only if hot, & restricted compositions)	✓ (only if hot)	✓ (only if hot)	✓ (only if hot)
	melt	× (fails Q-Vs constraint)	✓ (only if hot)	✓ (only if hot)	× (Vs too fast for melt)
	EA-GBS	× (too hot for EA-GBS)	× (Vs too fast for EA-GBS)	× (Vs too fast for EA-GBS)	× (Vs too fast for EA-GBS)
QYANG	*dry*	✓	✓	✓	✓
	damp	✓	✓	✓	✓
	wet	✓	✓	✓	✓
	melt	× (too cold for melt)	× (too cold for melt)	× (too cold for melt)	× (too cold for melt)
	EA-GBS	✓	× (too fast)	× (too fast)	× (too fast)

132 km		very slow	slow	fast	very fast
QBEHN	*dry*	× (crustal composition)	✓	✓	✓
	damp	× (crustal composition)	✓	✓	✓
	wet	× (crustal composition)	✓ (restricted compositions)	✓	✓
	melt	✓	✓	✓	✓ (v small %)
	EA-GBS	× (too hot)	× (too fast)	× (too fast)	× (too fast)
QYANG	*dry*	× (crustal composition)	✓ (only if cold, & restricted compositions)	✓ (only if cold)	✓ (only if cold)
	damp	× (crustal composition)	✓ (only if cold, & restricted compositions)	✓ (only if cold)	✓ (only if cold)
	wet	× (crustal composition)	✓ (only if cold, & restricted compositions)	✓ (only if cold)	✓ (only if cold)
	melt	× (too cold for melt)	× (too cold for melt)	× (too cold for melt)	× (too cold for melt)
	EA-GBS	✓ (only if cold)	× (Vs too fast for EA-GBS)	× (Vs too fast for EA-GBS)	× (Vs too fast for EA-GBS)

Note. The colors correspond to the color scheme used to distinguish dry, wet, damp, melting, and elastically accommodated grain boundary sliding models in Figures 8 and S1–S4. Weak shading (higher transparency) is used for models that are only acceptable under certain conditions (e.g., restricted range of temperature or composition).

geotherm; (3) the peridotite solidus under dry, damp, and wet conditions; and (4) the range of global mantle temperatures predicted by geodynamic modeling (Davies et al., 2012). This is shown in Figure 7.

Although our synthetic models have variable composition, the smaller sensitivity of V_s to composition than to T means that for most compositions, a 1300 °C (= 1573 K) adiabat falls close to that of pyrolite—typically less than ~50-K difference—and hence, it is meaningful to compare our models with the pyrolite adiabat.

4.1. Thermal Structure, Fluids, and Mechanical Properties at 52 km (Lithosphere)

In the case of the QBehn anelasticity correction, the temperatures of the synthetic models (~1300–1780 K) overlap with the 1300 °C pyrolite adiabat. With the exception of tectonically active regions (e.g., close to the mid-Atlantic ridge), this is very hot for 52-km depth and would likely place many of the models at temperatures above their solidus (see Figure 7). Away from tectonically active regions, a temperature profile closer to a conductive (lithospheric) geotherm (Figure 7) is more likely. Additionally, in the very slow regions, only the damp and wet models satisfy the constraint on Q and V_s (Figures S5 and S1a).

We found that if we instead apply the QYang anelasticity correction, it significantly reduces the temperatures required to fit the seismic data, and the model temperatures are then compatible with a conductive geotherm (see Figure 7). The QYang models fit the seismic data equally well, regardless of their water content (Figures S2a–S2d). We further note that the model temperatures are now consistent with EA-GBS, although this mechanism is not required to explain the seismic data. Furthermore, because the reduction in wave speed due to EA-GBS is very large, then this mechanism can only fit the data in very slow regions (where $V_s < 4.0$ km/s). EA-GBS models are associated with different chemical compositions (Mg richer and Si poorer) than the dry, damp, or wet models, whose compositions (Mg poorer and Si richer) are closer to crustal than mantle rocks (see Figure S2e).

In summary, it is possible to fit our seismic observations at 52 km entirely using the QYang anelasticity correction, if we assume that the temperatures everywhere are close to a conductive geotherm. However, in certain tectonic environments (e.g., hot spots and spreading centers), higher temperatures may arise, and in such environments, we must use the QBehn formalism instead to predict the correct temperatures. If we are in the regime of QBehn and the wave speeds are very slow (<4.0 km/s), then given the anticorrelation between $1/Q$ and V_s (equation (4)), water must be present; otherwise, Q becomes too high (Figures S5 and S1a). We find that partial melting is not required to explain the any of the wave speeds at this depth, although it is possible that there could be partial melting in addition to water in the hot regions where QBehn is required (note: It is not possible without water [see Figure S5] and we did not run a simulation with both water and partial melt, because we wanted to test if the individual mechanisms were required or preferred by the data).

4.2. Thermal Structure, Fluids, and Mechanical Properties at 132 km (Asthenosphere)

At 132 km, the QBehn synthetic models are again characterized by temperatures close to a Tp = 1300 °C adiabat (specifically, model temperatures lie in the range 1430–2000 K), while the QYang models are significantly colder (815–1260 K; see Figures 7 and S3 and S4). In *normal* asthenosphere, the QBehn model temperatures are more plausible, but in subduction environments, the temperatures predicted by QYang are also possible, and in fact both sets of models fall within the temperature ranges predicted by global geodynamic modeling at this depth (Figure 7). The most interesting feature at this depth, however, is the very slow regions where V_s is less than 4.0 km/s (see Figure 3 for their geographic locations). Using both the QBehn or QYang anelasticity corrections, we find that in order to reconstruct such low wave speeds under dry, damp, or wet conditions, our thermochemical models must have very specific chemical compositions (see Figure 8): low MgO and high SiO_2. These Mg/Si ratios are compatible with crustal rocks (oceanic and continental), but not with mantle rocks. We consider it unlikely that crustal rocks would be sufficiently abundant at 132-km depth to dominate the wave speeds at the resolution scales of seismic tomography (~100–200 km), and therefore, an alternative mechanism is required to explain the very slow wave speeds. In warm regions, this mechanism can be partial melting (with QBehn anelasticity parameters—see Figures S3a and S3e), and in cold regions, this mechanism can be EA-GBS (with QYang anelasticity parameters—see Figures S4a and S4e). Both of these mechanisms remove the dependence of V_s on composition (in other words, the output compositions are the same as the prior distributions; see Figure 8).

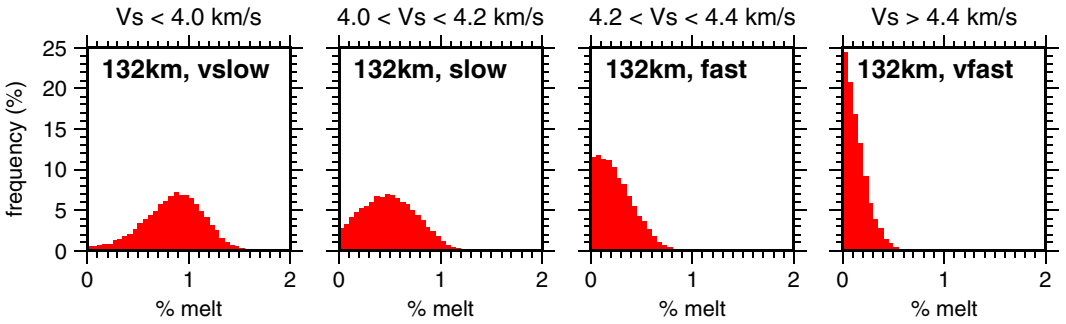

Figure 9. Distributions of melt fractions that can fit the wave speeds seen in tomography, for the simulations in which we allowed allocated a random melt fraction to each thermochemical model (i.e., *melt* models; section 2.4.3), after applying the Metropolis-Hastings algorithm, to fit the tomography V_S distributions (section 3.2). Histograms are shown for 132-km depth, and for each of the four *bands* of V_S spanned by the tomography model (illustrated in Figure 3). These distributions should not be interpreted as actual distributions of melt in the mantle but rather indicate the likelihood of a given melt fraction in that region, if we impose the condition that melting is present. We note that at all wave speeds, the existence of a small degree of melting is possible. The anelasticity correction is QBehn.

In the case of partial melting, a range of melt fractions are compatible with the data (shown in Figure 9), depending on the temperature and chemical composition. Assuming a melt sensitivity given by equation (3) (taken from Hammond and Humphreys, 2000b), the most likely melt fraction is about 0.8% (Figure 9).

4.3. The Importance of Chemical Composition

While placing a broad constraint on Q (equation (4)) allowed us to extract significant information about the mantle temperatures beneath Europe, the same cannot be said for composition, because there is no compositional dependence in the assumed parameterization for anelasticity (see equations (A1)–(A3)). At the same time, the chemical composition cannot be constrained using S wave speeds alone because the wave speeds are sensitive to both variations in composition and temperature, and these effects will "trade off" with each other. The result is that in general the chemical composition beneath Europe is poorly constrained (e.g., see the compositional ranges in Figures S1e–S1h, S2e–S2h, S3e–S3h, and S4e–S4h), although some trends are visible as the wave speed increases (the mean composition becomes more Mg rich, Si poor, and Fe poor). In order to better constrain the composition, we would require another independent observable such as P wave speed or density.

However, even though we often cannot constrain the composition, there are certain situations in which certain compositions are required by the tomography in order to explain the wave speeds (see Table 1 and Figure 8). Furthermore, by allowing the composition to vary in our modeling, we are able to demonstrate that at 132 km, the slowest regions of the tomography model are best explained by either partial melting or EA-GBS—which may not have been obvious, had a fixed chemical composition been assumed.

4.4. Wider Implications

One of the most striking results of our modeling is the importance of anelasticity parameters in determining the mantle temperature. Our two anelasticity models, QBehn and QYang, differ from each other only in two parameters: the frequency dependence α and the activation energy E. We therefore ran tests in which we adjusted only α, and only E, relative to QBehn (see red and purple bands, Figure 7). We found that most of the temperature difference between QBehn and QYang models is due to the reduction in α: If only E is changed, the model temperatures do not change (and in fact, in conjunction with equation (4), it is no longer possible to fit the slowest 50% of the tomography model). If only α is changed, the temperatures are reduced, but the combination of changing E and α together gives a larger reduction (see Figure 7).

In Figure 7 we plotted the temperature ranges of the QYang and QBehn models, and the range of upper mantle temperatures predicted by global geodynamic modeling (Davies et al., 2012). All of the QYang and QBehn models fall within the range of the geodynamic modeling, but neither covers the full range: QBehn models are at the hot end, and QYang models are at the cold end. The implication here is that in order to generate the full range of mantle temperatures predicted by geodynamics, α varies either with temperature or rheology.

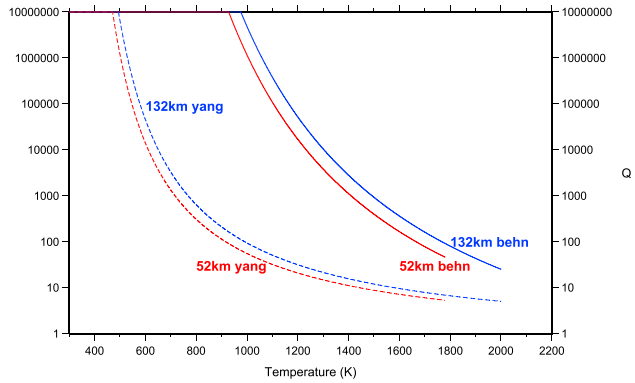

Figure 10. Q as a function of temperature for 4 million thermochemical models at 52-km depth (red lines) and 132 km (blue lines). The solid lines show the behavior for the QBehn anelasticity correction, and the dashed lines show the behavior for the QYang correction. In our modeling we only retained models with ~$23 < Q < 400$, resulting in a clear difference in temperature ranges between QBehn and QYang models. This plot shows that in order for the minimum temperature of the QBehn models to overlap with the maximum temperature of the QYang models at low Q, we would require the maximum Q to be of the order of 100,000 (at least).

The notion that α is variable is not new: Seismic observations have indicated that at mantle pressures α can range from −1.0 to +1.0 (Lekić et al., 2009; Romanowicz & Mitchell, 2007), although most observations are within the range 0.1–0.4. Lekić et al. (2009) suggested that the variation of α is frequency dependent, having observed a difference in α derived from normal modes (which predominantly sample the lower mantle), versus body and surface waves (which are more sensitive to shallow structure). In this study, we have shown that in the upper mantle α may also vary as a function of rheology and/or temperature. The value of α used in the QBehn correction ($\alpha = 0.27$) is taken from experimental observations of polycrystalline olivine (Faul & Jackson, 2005). This value is tightly constrained within the P,T conditions of the experiments but may change once extrapolated to mantle T and P (Lekić et al., 2009), and also for multimineralic assemblages, and so our inference does not contradict experimental data.

5. Discussion

5.1. Effect of the Q-V_s Constraint

To what extent does our interpretation depend on the assumed anticorrelation between $1/Q$ and V_s (i.e., equation (4))? Certainly, we need some information on Q, in order to make any inferences about the mantle temperature (see Figures 7 and S7 and S8). The anticorrelation defined by equation (4) allowed us both to obtain dynamically plausible mantle temperatures and to deduce the temperature dependence of α. This anticorrelation is based on the global surface wave data given in Figures 3 and 4 of Dalton et al. (2009), but we erred on the conservative side in defining the margin of uncertainty, so that it includes almost all the Q-V_s observations at 100-km depth and some window beyond this. We anticipate that this is a sufficiently cautious approach not to have overinterpreted their data.

As a further verification of our interpretation, we ran a second set of calculations, where instead of imposing an anticorrelation between $1/Q$ and V_s, we only retained models whose Q was between 40 and 400 (figures available on request). This second set of calculations was motivated by the values of Q that are seen in surface wave studies (Dalton et al., 2009): The vast majority of shallow mantle observations of Q from surface waves are in the range 40–200, although higher values of the order of 500–1,500 are sometimes seen in continental shields (Alice et al., 2017; e.g., Dalton & Faul, 2010; Dalton et al., 2017). Dalton et al. (2009) is one of the most comprehensive global studies of Q. In this compilation, the absolute maximum is around 5,000. The minimum is at around 40. With this different (but overlapping) constraint on Q, our conclusions were very similar, with only minor differences regarding the relative importance of water versus partial melting at shallower depths. The conclusions that α is temperature (or rheology) dependent and partial melting or EA-GBS are required at 132 km remained.

One of the major consequences of restricting Q (either by correlating it with V_s or limiting its minimum and maximum values) is that it places a major restriction on the temperatures of the models that are compatible with the seismic data. With both of the restrictions that we imposed, we found that the QBehn anelasticity correction (where $\alpha = 0.27$) gave unrealistically high temperatures at 52 km (but reasonable at 132 km), while the QYang correction (where $\alpha = 0.1$) gave more reasonable temperatures at 52 km (but cold at 132 km)—and so we have suggested that α varies with temperature and/or rheology. But how strongly is our interpretation tied to our assumptions about Q? Most of our accepted thermochemical models are associated with $Q < 200$. This happens even though both Q constraints allow maximum values up to ~350–400. In Figure 10 we show Q as a function of temperature for the thermochemical models. From this plot, we can see that if we would change the upper bound of Q to 1,000, it reduces the minimum temperature of the models only by about 50 K. This would not be enough to change our conclusions. If we would want to reduce the temperatures so much that the values coming from QBehn overlap with those of the QYang correction at low Q, we would require Q values of the order of 10^5 or higher. Based on the information that we have from surface wave studies, we do not have

any evidence that Q should be so high, and that is why we suggested that there may be a different frequency dependence for Q in the lithosphere versus the asthenosphere.

In other words, our interpretation does not depend on the assumed upper limit of Q.

However, the imposed lower limit on Q does have a significant impact, especially regarding inferences about melt and EA-GBS (the minimum Q permitted by equation (4) is about 23). In previous studies of mid-ocean ridges, there has been a debate regarding the origin of low (i.e., ~4.2 km/s and slower) wave speeds at asthenospheric depths. For example, in the East Pacific Rise, Yang et al. (2007) suggested that partial melting was required to explain the slowest regions, while Goes et al. (2012) showed with thermodynamic modeling that the observed wave speeds could be reconstructed with reasonable temperatures purely by accounting for anelasticity. Goes et al. (2012) tested a number of different anelasticity corrections including the QBehn and QYang formalisms. However, their preferred thermal model requires Q values in the range 5–20. It is likely that similarly low Q values are required in other studies that have implicated anelasticity without melt to explain low wave speeds (e.g., Priestley & McKenzie, 2006), although the Q model is not explicitly given in these cases. Our tomography model is derived from surface waves that deliver a minimum spatial resolution (laterally) of the order of a few hundred kilometers (Fichtner & Trampert, 2011). At the frequencies of the seismic waves, Q cannot be so low because then the surface waves on which our model is built would disappear. Hence our assumed lower limit for Q is reasonable (although it is possible that lower values of Q may exist punctually, and they may be detected by other observables than surface waves).

We note also that our interpretation is consistent with the study of Abers et al. (2014) who combined observations of Q with petrological constraints in various back arc and subarc mantle regions. Their observations of Q, in the range 25–80 (so not exceptionally low), were best explained by partial melting between 50- and 100-km depth.

5.2. Choice of Tomography Model

In addition to the tomography model of Fichtner et al. (2013), an alternative full waveform tomography model for Europe has been developed by H. Zhu and coworkers (Zhu et al., 2015; Zhu et al., 2012; Zhu et al., 2013). If we compare the models of Fichtner et al. (2013) and Zhu et al. (2015) at 132 km, the range and distribution of the wave speeds are in good agreement (see Figure 11). However, the model of Fichtner et al. is systematically slower than Zhu et al., by approximately 0.28 km/s at 130-km depth. Most of this difference can be accounted for by the fact that Fichtner et al.'s model is presented in a relaxed state (we have chosen the minimum frequency of the numerical absorption band, 0.01 Hz, to represent this relaxed state). Zhu et al. (2015) used SPECFEM3D to compute their model. In SPECFEM3D, the models are expressed at a reference frequency also defined by the implemented absorption band. We checked in the code and found that Zhu et al.'s model is given at a reference frequency of close to 1 Hz. In that case, for a given Q value, the dispersion due to attenuation would cause the wave speeds of the two models to differ by ~0.2 km/s. The rest of the difference between the models may be accounted for by their different spatial resolutions (horizontally and vertically) and different ranges of latitude and longitude.

We based our study on the model of Fichtner et al. because we know the full details of the inversion procedure, including the frequency. It is essential that we know both the frequency, and how to account for Q, in order to correctly compare between the mineral wave speeds derived in mineral physics, and those observed in seismology. However, we note that if we systematically shift the model of Zhu et al. to be ~ 0.3 km/s slower, and perform the same calculations, following the same assumptions about the relation between Q and V_s, then our interpretation does not change.

At 52 km, the two tomography models differ from each other substantially, and this is due to the way in which crustal structure has been implemented. In Fichtner et al. (2013), crustal structure was accounted for with a *seismically equivalent crust* placed above 50-km depth, meaning that the mapped structure at 52 km ought to represent the mantle (although there may be exceptions, e.g., the Himalayas/Tibet). In Zhu et al. (2015) the crustal model EPcrust (Molinari & Morelli, 2011) was used as the starting model, with the result that the Moho exceeds 50 km in many parts of central and eastern Europe (NB their model does not extend as far east as Tibet). Clearly, in order to make inferences about melting and grain-boundary sliding, it is important to ascertain if we are in the crust or the mantle, and better constraints on this could have implications for our interpretation.

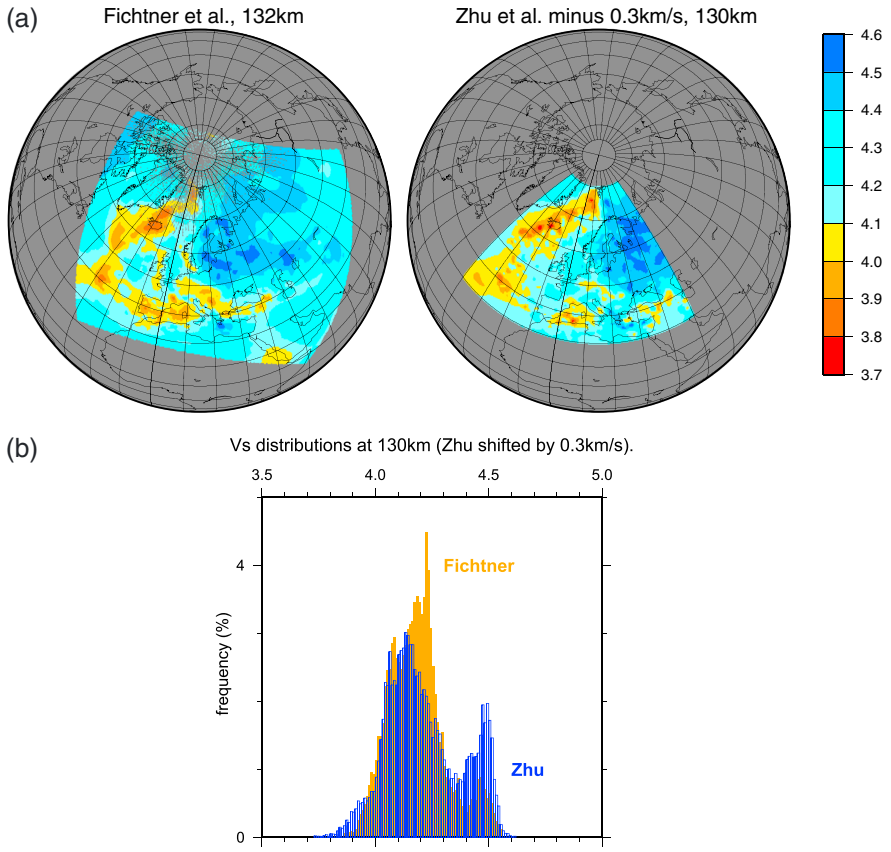

Figure 11. Comparison of the two full waveform tomography models for Europe (Fichtner et al., 2013; Zhu et al., 2015) at 132- and 130-km depth, where the model of Zhu et al. (2015) has been shifted systematically to 0.3 km/s slower. (a) Maps of absolute V_S. (b) Histograms of the V_S distributions, in which the (i) V_S of Zhu et al. has been reduced by 0.3 km/s and (ii) for the model of Fichtner et al., only latitudes and longitudes that overlap with Zhu et al. are included. There is good agreement in the shape and ranges of the two V_S distributions.

Recently, Zhu and coworkers have been developing a 3-D attenuation (or *Q*) model for Europe (Zhu et al., 2013, 2015). At the depth range of interest for this study, further refinement of the attenuation model is, however, needed before it can be applied in a quantitative interpretation. Although we could not implement a *Q* model consistent with the seismic model in our investigation, we have highlighted precisely why seismic tomography should be working toward better constraining the 3-D *Q* structure and hence the value of studies like Zhu et al. (2015).

5.3. Uncertainties in Model Melt Fractions

Our correction for melt is based on numerical modeling (Hammond & Humphreys, 2000a, 2000b), and we assumed a sensitivity of *S* wave speed to melt fraction of −7.9% per 1% melt. This is a purely mechanical correction and accounts for velocity weakening due to viscous shear relaxation and melt squirt. It does not consider melt-induced grain-boundary sliding, which may further weaken the velocities and hence require a smaller melt fraction than we inferred to produce a given velocity reduction. Recent experimental observations of partially molten basalt (Clark et al., 2016; Freitas et al., 2017) have inferred *S* wave sensitivities to melt that are similar to those assumed in our modeling, for melt fractions below 0.85%. At larger melt fractions, experiments indicate that the sensitivity increases. Hence, there is some evidence that the true sensitivity may be underestimated in this study, and in that case, smaller melt fractions would be required to generate a given wave speed reduction.

5.4. Melting or EA-GBS at 132 km?

We have demonstrated that the very slow regions of the tomography model at 132-km depth require either partial melting up to ~0.5–1.5% (if it is warm; Figure 9) or EA-GBS (if it is cold). On the basis of electrical

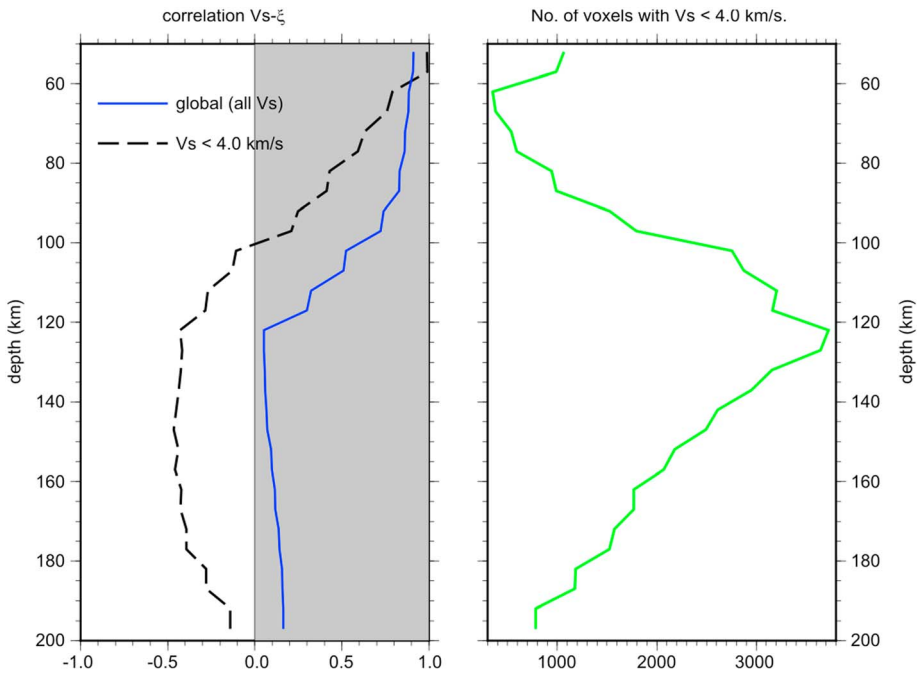

Figure 12. (left) Correlation between V_S and radial anisotropy $\xi = \frac{V_{SH}^2}{V_{SV}^2}$ as a function of depth, for all regions in the tomography model (blue line), and only those regions where V_S is <4.0 km/s (black dashed line). (right) Count of the number of voxels at each depth in the tomography model for which V_S is <4.0 km/s.

conductivity observations and petrological and geodynamic models, Karato (2014) argues that melt fractions probably do not exceed ~0.1% away from shallow mid-ocean ridges, and thus, EA-GBS may offer a more plausible explanation for slow wave speeds. For Europe, our preferred interpretation is for partial melting, because many of the very slow regions are close to the Iceland and Azores plumes (Figure 3), where high temperatures are likely. That being said, a second band of very slow wave speeds occurs in parts of Iberia and the Mediterranean. If there would be cold remnants of subducted material in these places (associated with convergence between Europe and Africa), then EA-GBS would be a viable mechanism for generating the low wave speeds. However, since the slowest wave speeds of the tomography model peak in abundance in a particular depth interval (~120–140 km, Figure 2), it implies that they have a common origin, and the cold temperatures required for EA-GBS are not likely beneath Iceland and Azores.

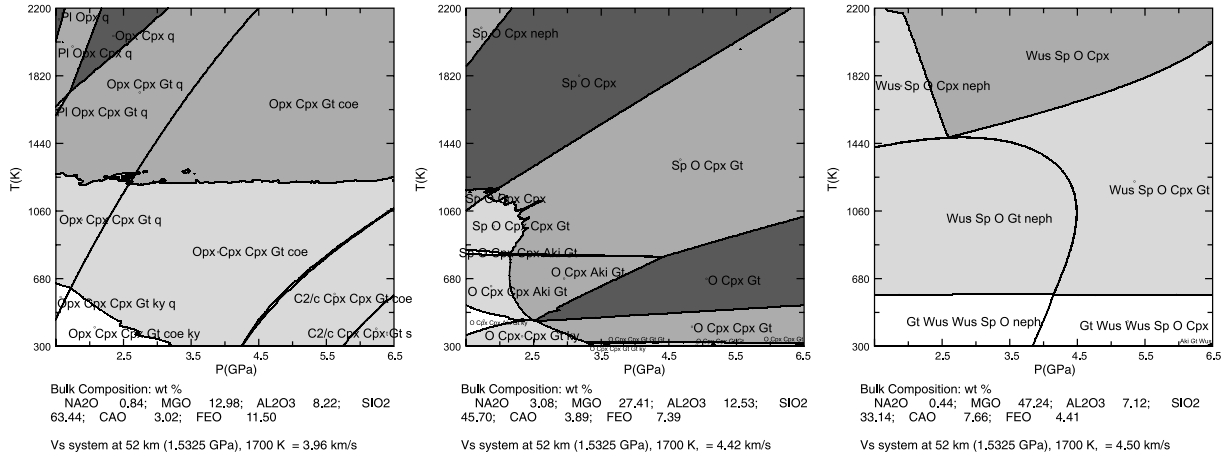

Figure 13. Some example phase diagrams of thermochemical models with increasing Mg/Si ratio and decreasing V_S from left to right. Note the stated V_S values are the anharmonic V_S (i.e., before any correction for anelasticity).

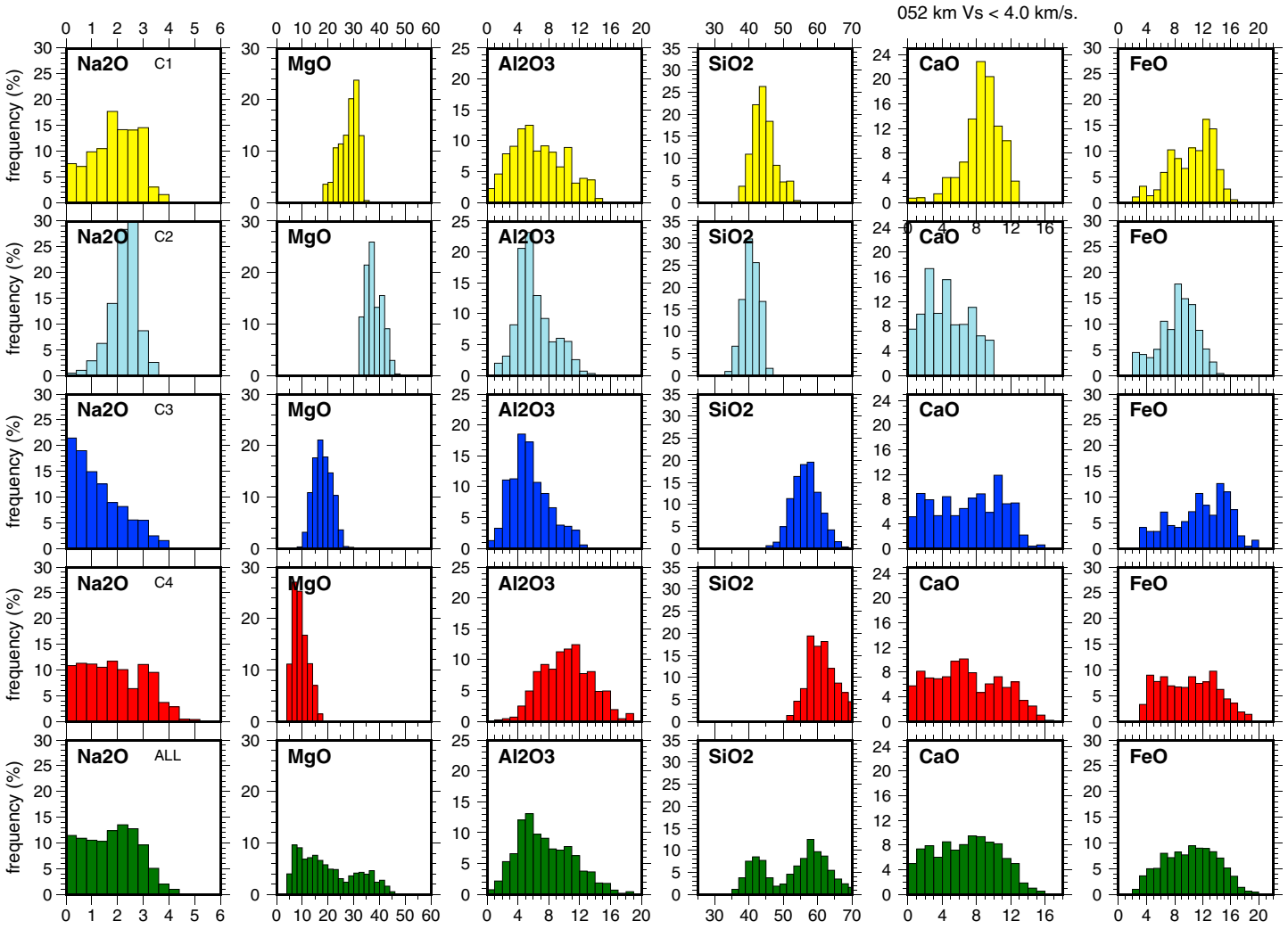

Figure 14. We performed a cluster analysis to test which of the six oxides are most influential on the wave speed (using the *dry* models plotted in Figure S2). The models are divided into four groups (C1, C2, C3, and C4) on the basis of their chemical composition only. Above, we show the compositional ranges of each cluster (a different color is used for each cluster). The bottom row (green) shows the original distributions before cluster analysis.

Additionally, partial melting may be compatible with anisotropy constraints (see Figure 12): Our isotropic V_s model was created by combining Vs_H and Vs_V, assuming: $V_s = \frac{1}{3}V_{S_v} + \frac{2}{3}V_{S_H}$, and so we can study its radial anisotropy in the form of $\xi = \frac{V_{S_H}^2}{V_{S_V}^2}$. We are cautious about interpreting this anisotropy, since Vs_H and Vs_V may not sample the region with the same spatial resolution. Nevertheless, below 100 km (and extending to ~200 km), while the average radial anisotropy in the tomography model remains close to zero, the slow regions ($V_s < 4$ km/s) are anticorrelated with ξ, in other words V_s is low when ξ is high. Kawakatsu et al. (2009) proposed that partial melting combined with shear deformation, in the lithosphere-asthenosphere transition region, can allow significant melt fractions to accumulate in horizontal layers, surrounded by melt-free mantle. At a large scale, the average melt fraction may be small (<1%) even if the melt-rich layers have a high melt fraction, but the alternation of melt-rich and melt-poor layers would produce significant radial anisotropy, with $Vs_H > Vs_V$, and hence, a high ξ. Here the anticorrelation reaches a maximum at around 120 km (with a value of approximately −0.4)—the same depth at which the slow regions occupy the biggest horizontal area. In other words, if there would be anisotropy due to horizontal melt-rich layers, these are spatially correlated with the regions of the tomography model in which the isotropic *S* wave speeds also suggest the presence of partial melting.

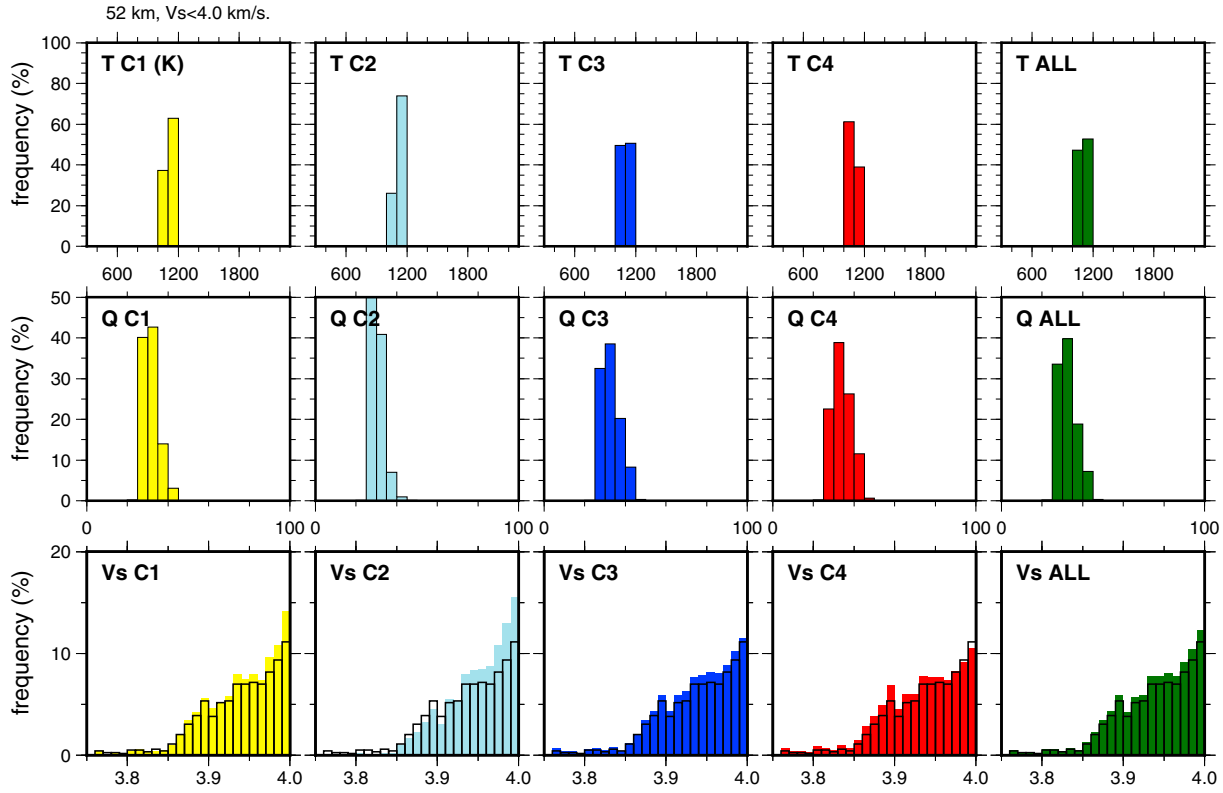

Figure 15. Distributions of temperature, Q, and V_S for the four clusters shown in Figure 14. The S wave speeds are influenced by the Mg/Si ratio (e.g., compare C2 here, and in Figure 14, with the other clusters). Note that temperature was excluded from this cluster analysis. If temperature is included in the analysis, we also observe a trade-off between temperature and FeO content.

In our study we considered various velocity-weakening effects (water, melt, and EA-GBS) separately, to test which ones are required by the data. It is of course possible that two or more of these processes may occur simultaneously. In order to determine their relative contribution to a given V_s, we would require additional information. In particular, knowledge of the local, 3-D Q structure and α would provide an even stronger constraint on the temperature, which would allow us to distinguish melt from EA-GBS (and provide more insight into the water content). A more detailed knowledge of V_P and density would put more constraints on the composition, which in turn might also put tighter constraints on the velocity-weakening processes.

5.5. Mineral Assemblages of the Thermochemical Models

Throughout this study we parameterized the chemical compositions of our models as a function of six oxides, as opposed to mineral proportions. While the former parameterization is more efficient (computationally), the latter is more amenable to petrological interpretation. Since, however, we cannot place tight constraints on the composition expressed as relative proportions of the mineral oxides (Figures S1e–S1h, S2e–S2h, S3e–S3h, and S4e–S4h), there is little to be gained by presenting a detailed analysis of the corresponding mineral proportions. Some example phase diagrams for varying Mg/Si ratio are shown in Figure 13, together with a *k* means cluster analysis of the QYang very slow models at 52-km depth (Figures 14 and 15; the precluster analysis models were plotted in Figures S2a and S2e).

The dominant signal in the cluster analysis is a division into groups of Mg-poor, Si-rich models (clusters C3 and C4, Figure 14) and a group of Mg-richer, Si-poorer models (cluster C2). (There is also a cluster with intermediate MgO and SiO_2 content and high FeO, cluster C1.) In the models with higher Mg/Si, the mineralogy (at 52 km) is mostly olivine and (clino) pyroxene, with small amounts of spinel and sometimes magnesiowüstite. In the models with low Mg/Si, olivine (and spinel and magnesiowustite) disappear, and instead we see (at 52 km) orthopyroxene, plagioclase, and quartz. These three minerals are all slower than olivine (and spinel and magnesiowustite) leading to slower S wave speeds in the bulk assemblage (see Figures 14 and 15—

compare the wave speed distributions of C2 [high Mg/Si models] and C4 [low Mg/Si models]). It is thus these two different mineral assemblages that give rise to the bimodal distributions of MgO and SiO_2 content when observing all models together (bottom row, Figure 14).

6. Concluding Remarks

We have demonstrated that working with only an *S* wave speed tomography model, together with a very broad constraint on the seismic attenuation, allows us to make significant inferences about the thermal state of the mantle and associated dynamic behavior such as partial melting or grain-boundary sliding. However, ongoing (and future) efforts in seismology to constrain the mantle attenuation structure at a regional scale in three dimensions will be of immense value for better distinguishing between different velocity-weakening mechanisms. Furthermore, our results indicate that the frequency dependence of the shear anelasticity α is itself rheology or temperature dependent, with higher values (~0.3) more appropriate in the asthenosphere and lower values (~0.1) more appropriate in the lithosphere.

Appendix A

A1. Anelasticity Correction

In general the effect of anelasticity on V_s may be expressed as (e.g., Karato, 1993):

$$Vs_{\text{anel}} = Vs_{\text{anh}}\left(1 - \frac{Q^{-1}(\omega, T, P, C_{\text{OH}}, d)}{2\tan(\pi\alpha/2)}\right) \tag{A1}$$

where Vs_{anh} is the (anharmonic) *S* wave speed at infinite frequency; Q is the quality factor, dependent on pressure, temperature, seismic frequency ω, water concentration C_{OH}, and grain size d; and α is a dimensionless constant.

We used the formulation of Behn et al. (2009) to calculate Q:

$$Q^{-1} = \left(Bd^{-G}\omega^{-1}\exp\left(-\frac{E + \text{PV}}{\text{RT}}\right)\right)^{\alpha} \tag{A2}$$

with B, the preexponential factor, given by

$$B = B_0 d_{\text{ref}}^{G-G_{\text{ref}}}\left(\frac{C_{\text{OH}}}{C_{\text{OH(ref)}}}\right)^{r}\exp\left(\frac{(E + P_{\text{ref}}V) - (E_{\text{ref}} + P_{\text{ref}}V_{\text{ref}})}{\text{RT}_{\text{ref}}}\right) \tag{A3}$$

where the subscript *ref* indicates reference values derived from experimental observations (see Behn et al., 2009), R is the gas constant, E is the activation energy, $V$is the activation volume, G is a dimensionless constant describing the grain size dependence, and r is a dimensionless constant describing the dependence of Q on water content, with a value between 1 and 2 (e.g., Shito et al., 2006).

For most parameters we used the values given in Behn et al. (2009), which are based on fitting experimental constraints:

α = 0.27
B_0 = 1.28×10^8 m/s
d_{ref} = 1.24×10^{-5} m
$C_{\text{OH(ref)}}$ = 50H/10^6Si
T_{ref} = 1538 K
P_{ref} = 3.0×10^5 kPa
G_{ref} = 1.09
E_{ref} = 505 kJ/mol
V_{ref} = 1.2×10^{-5} m^3/mol

G = 1.00
E = 420 kJ/mol
V = 1.2×10^{-5} m^3/mol

And assumed the following values for the remaining parameters:
ω = 0.01 Hz (to match the frequency at which the tomography model was calculated)
d = 1.0×10^{-2} m (according to Behn et al., 2009, in the shallow upper mantle, grain sizes are likely in the range 1–100 mm. We found that the dependence of Vs_{anel} on grain size, within this range of d values, was small compared to other parameters and therefore opted to use an intermediate grain size of 10 mm for our simulations)
C_{OH} = 50H/10^6Si for *dry* mantle or
C_{OH} = 1,000H/10^6Si for *damp* mantle. According to Behn et al. (2009), upper mantle water content is likely to vary between 50 and 2,000H/10^6Si or
C_{OH} = 3,000H/10^6Si for *wet* mantle (a maximum water concentration, suggested by Goes et al., 2012)
r = 0 for dry mantle or
r = 1 for damp mantle
r = 2 for wet mantle—chosen to maximize the sensitivity of V_s to water

P is given by the particular depth of the tomography model, which we are trying to interpret, using the depth-pressure calibration of PREM (Dziewonski & Anderson, 1981), and T is the randomly chosen temperature of that particular simulation. We tested that with this particular formulation, changing the mineral grain size does not significantly modify Q.

A2. Correction for Elastically Accommodated Grain-Boundary Sliding

The characteristic frequency at which EA-GBS is activated, ω_{EAGBS}, is given by (Karato et al., 2015)

$$\omega_{EAGBS} = A \cdot d^{-1} \cdot \exp\left(\frac{E^* + PV^*}{RT}\right) \cdot \left[1 + \left(\frac{C_w}{C_{w0}}\right)^r\right] \quad \text{(A4)}$$

where A is a constant, C_w is the water content, C_{w0} is the water content at which wet behavior changes to dry behavior, and all other parameters are as defined for equation (A3).

Using equation (A4) and the reference values given in Karato et al. (2015), we calculated the characteristic frequency for each of our thermochemical models (with the temperature T being the parameter which varies between models). We only retained models for which this frequency was between 0.01 and 0.125 Hz (i.e., 8 to 100 s), corresponding to the range of seismic frequencies occurring in both the original seismic data and the derived tomography model. For clarification, the reference values are as follows:
A = 2.3×10^{14} s^{-1} m
C_{w0} = 10^{-4} wt %
r = 1
E^* = 350 kJ/mol
V^* = 10^{-6} m^3
d = 5×10^{-3} m

And we assumed
C_w = 10^{-6} wt % (essentially dry mantle)
ω_{EAGBS} = 0.01 Hz

The reference values in Karato et al. (2015) are based on a statistical analysis (Olugboji et al., 2013) of experimental data (Faul & Jackson, 2005; Jackson & Faul, 2010). We note a minor inconsistency in our calculation, in that these reference values were obtained at a frequency of 0.1 Hz, but we consider a range of frequencies.

From those models with appropriate characteristic frequencies, we then made another selection on the basis of temperature—only keeping those whose temperatures fall within the ranges shown in Figure 3 of Karato et al. (2015). This meant that at 52 km, we kept models with temperatures between 900 and 1120 K, and at 132 km, we kept models with temperatures between 1080 and 1300 K.

The V_s of these models were then corrected for anelasticity using equations (A1)–(A3). All parameters were kept the same as before, except for d (grain size), which we assumed to be 5 mm, in order to be consistent with the grain size of 5 mm applied in (A4).Since the seismic velocities depend only weakly on grain size, this small adjustment does not affect our interpretation. We then corrected Vs_{anel} for EA-GBS. Experimental studies do not yet give consistent results for the effect of EA-GBS on seismic wave speeds, with the magnitude of velocity reduction estimated to be between 10 and 40%. Karato et al. (2015) list three possible formulations for the velocity reduction, and we tested all of them:

$$Vs_{\mathrm{gbs1}} = Vs_{\mathrm{anel}} \cdot \frac{2}{5} \cdot \frac{7+5\upsilon}{7-4\upsilon} \quad \text{(A5)(Zener)}$$

$$Vs_{\mathrm{gbs2}} = Vs_{\mathrm{anel}} \cdot \sqrt{\frac{1}{[0.57 \cdot (1-\upsilon)+1]}} \quad \text{(A6)(RajAshby)}$$

$$Vs_{\mathrm{gbs3}} = Vs_{\mathrm{anel}} \cdot \sqrt{\frac{0.86-0.83\upsilon}{1-\upsilon} \cdot \frac{1+\upsilon}{1.14+0.83\upsilon}} \quad \text{(A7)(Ghahremani)}$$

where υ is Poisson's ratio $\frac{Vp^2-2Vs^2}{2(Vp^2-Vs^2)}$ and Vp and Vs are the unrelaxed P and S wave speeds (i.e., prior to any correction for anelasticity) of the thermochemical model, calculated using *Perple_X*.

The first formulation (gbs1, equation (A5) (Zener)) produced such a large velocity reduction that the thermochemical models all become slower than anything in the tomography model and was no longer considered. The second and third formulations (gbs2 and gbs3, equations (A6) (RajAshby) and (A7) (Ghahremani), respectively) both produce less extreme velocity reductions, with gbs2 having a bigger effect than gbs3. While gbs2 can produce velocities compatible with the very slowest parts of the tomography model, they are not fast enough to cover the whole of the slowest band ($V_s \leq 4.0$ km/s) into which we divided our model, and so in the figures we only show the results for gbs3.

Acknowledgments

L. C. and A. F. were supported by the Dutch Science Foundation (NWO) on Grant NWO: VIDI 864.11.008. The research leading to these results also received funding from the European Research Council under the European Union's Seventh Framework Programme (FP/2007–2013)/ERC Grant Agreement 320639. We thank the Editor and two anonymous reviewers for their helpful comments that enabled us to improve the manuscript. This work represents a statistical interpretation of a full waveform tomography model (Fichtner et al., 2013) in terms of temperature, composition, melting, and velocity-weakening mechanisms. All randomly generated thermochemical models, as well as the tomography model, can be found at http://www.geo.uu.nl/~jeannot/My_web_pages/Downloads.html. The thermochemical models were generated using *Perple_X* (Connolly, 1990, 2005). All histograms were generated with the "pshistogram" command from the GMT package (https://www.soest.hawaii.edu/gmt/). The importance sampling was performed using a Metroplis-Hastings algorithm described in Mosegaard and Tarantola (1995), Cobden et al. (2012), and Mosca et al. (2012).

References

Abers, G. A., Fischer, K. M., Hirth, G., Wiens, D. A., Plank, T., Holtzman, B. K., et al. (2014). Reconciling mantle attenuation-temperature relationships from seismology, petrology, and laboratory measurements. *Geochemistry, Geophysics, Geosystems*, *15*, 3521–3542. https://doi.org/10.1002/2014GC005444

Afonso, J. C., Fullea, J., Griffin, W. L., Yang, Y., Jones, A. G., Connolly, J. A. D., & O'Reilly, S. Y. (2013). 3-D multiobservable probabilistic inversion for the compositional and thermal structure of the lithosphere and upper mantle. I: A priori petrological information and geophysical observables. *Journal of Geophysical Research: Solid Earth*, *118*, 2586–2617. https://doi.org/10.1002/jgrb.50124

Alice, A., Eric, D., & Yanick, R. (2017). Attenuation tomography of the upper mantle. *Geophysical Research Letters*, *44*, 7715–7724. https://doi.org/10.1002/2017GL073751

Anderson, D. L., & Given, J. W. (1982). Absorption band Q model for the Earth. *Journal of Geophysical Research*, *87*(B5), 3893–3904. https://doi.org/10.1029/JB087iB05p03893

Anderson, D. L., & Sammis, C. (1970). Partial melting in the upper mantle. *Physics of the Earth and Planetary Interiors*, *3*, 41–50. https://doi.org/10.1016/0031-9201(70)90042-7

Behn, M. D., Hirth, G., & Elsenbeck, J. R. II (2009). Implications of grain size evolution on the seismic structure of the oceanic upper mantle. *Earth and Planetary Science Letters*, *282*(1–4), 178–189. https://doi.org/10.1016/j.epsl.2009.03.014

Cammarano, F., Goes, S., Vacher, P., & Giardini, D. (2003). Inferring upper-mantle temperatures from seismic velocities. *Physics of the Earth and Planetary Interiors*, *138*(3-4), 197–222. https://doi.org/10.1016/S0031-9201(03)00156-0

Clark, A. N., Lesher, C. E., Jacobsen, S. D., & Wang, Y. (2016). Anomalous density and elastic properties of basalt at high pressure: Reevaluating of the effect of melt fraction on seismic velocity in the Earth 's crust and upper mantle. *Journal of Geophysical Research: Solid Earth*, *121*, 4232–4248. https://doi.org/10.1002/2016JB012973

Cobden, L., Goes, S., Cammarano, F., & Connolly, J. A. (2008). Thermochemical interpretation of one-dimensional seismic reference models for the upper mantle: Evidence for bias due to heterogeneity. *Geophysical Journal International*, *175*(2), 627–648. https://doi.org/10.1111/j.1365-246X.2008.03903.x

Cobden, L., Goes, S., Ravenna, M., Styles, E., Cammarano, F., Gallagher, K., & Connolly, J. A. (2009). Thermochemical interpretation of 1-D seismic data for the lower mantle: The significance of nonadiabatic thermal gradients and compositional heterogeneity. *Journal of Geophysical Research*, *114*, B11309. https://doi.org/10.1029/2008JB006262

Cobden, L., Mosca, I., Trampert, J., & Ritsema, J. (2012). On the likelihood of post-perovskite near the core–mantle boundary: A statistical interpretation of seismic observations. *Physics of the Earth and Planetary Interiors*, *210*, 21–35.
Connolly, J. A. D. (1990). Multivariable phase-diagrams—An algorithm based on generalized thermodynamics. *American Journal of Science*, *290*(6), 666–718. https://doi.org/10.2475/ajs.290.6.666
Connolly, J. A. D. (2005). Computation of phase equilibria by linear programming: A tool for geodynamic modeling and its application to subduction zone decarbonation. *Earth and Planetary Science Letters*, *236*(1–2), 524–541. https://doi.org/10.1016/j.epsl.2005.04.033
Dalton, C. A., Bao, X., & Ma, Z. (2017). The thermal structure of cratonic lithosphere from global rayleigh wave attenuation. *Earth and Planetary Science Letters*, *457*, 250–262. https://doi.org/10.1016/j.epsl.2016.10.014
Dalton, C. A., Ekström, G., & Dziewonski, A. M. (2009). Global seismological shear velocity and attenuation: A comparison with experimental observations. *Earth and Planetary Science Letters*, *284*(1–2), 65–75. https://doi.org/10.1016/j.epsl.2009.04.009
Dalton, C. A., & Faul, U. H. (2010). The oceanic and cratonic upper mantle: Clues from joint interpretation of global velocity and attenuation models. *Lithos*, *120*, 160–172. https://doi.org/10.1016/j.lithos.2010.08.020
Davies, D. R., Goes, S., Davies, J. H., Schuberth, B., Bunge, H., & Ritsema, J. (2012). Reconciling dynamic and seismic models of Earth's lower mantle: The dominant role of thermal heterogeneity. *Earth and Planetary Science Letters*, *353*, 253–269.
Deschamps, F., Cobden, L., & Tackley, P. J. (2012). The primitive nature of large low shear-wave velocity provinces. *Earth and Planetary Science Letters*, *349*, 198–208.
Deschamps, F., & Trampert, J. (2003). Mantle tomography and its relation to temperature and composition. *Physics of the Earth and Planetary Interiors*, *140*(4), 277–291. https://doi.org/10.1016/j.pepi.2003.09.004
Durek, J. J., & Ekström, G. (1996). A radial model of anelasticity consistent with long-period surface-wave attenuation. *Bulletin of the Seismological Society of America*, *86*(1A), 144–158.
Dziewonski, A. M., & Anderson, D. L. (1981). Preliminary reference Earth model. *Physics of the Earth and Planetary Interiors*, *25*(4), 297–356. https://doi.org/10.1016/0031-9201(81)90046-7
Faul, U. H., & Jackson, I. (2005). The seismological signature of temperature and grain size variations in the upper mantle. *Earth and Planetary Science Letters*, *234*(1–2), 119–134. https://doi.org/10.1016/j.epsl.2005.02.008
Fichtner, A., & Trampert, J. (2011). Resolution analysis in full waveform inversion. *Geophysical Journal International*, *187*(3), 1604–1624. https://doi.org/10.1111/j.1365-246X.2011.05218.x
Fichtner, A., Trampert, J., Cupillard, P., Saygin, E., Taymaz, T., Capdeville, Y., & Villaseñor, A. (2013). Multiscale full waveform inversion. *Geophysical Journal International*, *194*(1), 534–556. https://doi.org/10.1093/gji/ggt118
Freitas, D., Manthilake, G., Schiavi, F., Chantel, J., Bolfan-Casanova, N., Bouhifd, M., & Andrault, D. (2017). Experimental evidence supporting a global melt layer at the base of the Earth's upper mantle. *Nature Communications*, *8*(1), 2186. https://doi.org/10.1038/s41467-017-02275-9
French, S. W., & Romanowicz, B. (2015). Broad plumes rooted at the base of the Earth's mantle beneath major hotspots. *Nature*, *525*(7567), 95–99. https://doi.org/10.1038/nature14876
Goes, S., Armitage, J., Harmon, N., Smith, H., & Huismans, R. (2012). Low seismic velocities below mid-ocean ridges: Attenuation versus melt retention. *Journal of Geophysical Research*, *117*, B12403. https://doi.org/10.1029/2012JB009637
Goes, S., Govers, R., & Vacher, P. (2000). Shallow mantle temperatures under Europe from P and S wave tomography. *Journal of Geophysical Research*, *105*(B5), 11,153–11,169. https://doi.org/10.1029/1999JB900300
Hammond, W. C., & Humphreys, E. D. (2000a). Upper mantle seismic wave attenuation: Effects of realistic partial melt distribution. *Journal of Geophysical Research*, *105*(B5), 10,987–10,999. https://doi.org/10.1029/2000JB900042
Hammond, W. C., & Humphreys, E. D. (2000b). Upper mantle seismic wave velocity: Effects of realistic partial melt geometries. *Journal of Geophysical Research*, *105*(B5), 10,975–10,986. https://doi.org/10.1029/2000JB900041
Hieronymus, C. F., & Goes, S. (2010). Complex cratonic seismic structure from thermal models of the lithosphere: Effects of variations in deep radiogenic heating. *Geophysical Journal International*, *180*(3), 999–1012. https://doi.org/10.1111/j.1365-246X.2009.04478.x
Jackson, I., & Faul, U. H. (2010). Grainsize-sensitive viscoelastic relaxation in olivine: Towards a robust laboratory-based model for seismological application. *Physics of the Earth and Planetary Interiors*, *183*(1–2), 151–163. https://doi.org/10.1016/j.pepi.2010.09.005
Jackson, I., Gerald, F., John, D., Faul, U. H., & Tan, B. H. (2002). Grain-size-sensitive seismic wave attenuation in polycrystalline olivine. *Journal of Geophysical Research*, *107*(B12), 2360. https://doi.org/10.1029/2001JB001225
Karato, S. (1993). Importance of anelasticity in the interpretation of seismic tomography. *Geophysical Research Letters*, *20*(15), 1623–1626. https://doi.org/10.1029/93GL01767
Karato, S. (2012). On the origin of the asthenosphere. *Earth and Planetary Science Letters*, *321-322*, 95–103. https://doi.org/10.1016/j.epsl.2012.01.001
Karato, S. (2014). Does partial melting explain geophysical anomalies? *Physics of the Earth and Planetary Interiors*, *228*, 300–306. https://doi.org/10.1016/j.pepi.2013.08.006
Karato, S., Olugboji, T., & Park, J. (2015). Mechanisms and geologic significance of the mid-lithosphere discontinuity in the continents. *Nature Geoscience*, *8*(7), 509–514. https://doi.org/10.1038/NGEO2462
Karato, S., & Spetzler, H. A. (1990). Defect microdynamics in minerals and solid-state mechanisms of seismic wave attenuation and velocity dispersion in the mantle. *Reviews of Geophysics*, *28*(4), 399–421. https://doi.org/10.1029/RG028i004p00399
Katz, R. F., Spiegelman, M., & Langmuir, C. H. (2003). A new parameterization of hydrous mantle melting. *Geochemistry, Geophysics, Geosystems*, *4*(9), 1073. https://doi.org/10.1029/2002GC000433
Kawakatsu, H., Kumar, P., Takei, Y., Shinohara, M., Kanazawa, T., Araki, E., & Suyehiro, K. (2009). Seismic evidence for sharp lithosphere-asthenosphere boundaries of oceanic plates. *Science*, *324*(5926), 499–502. https://doi.org/10.1126/science.1169499
Lekić, V., Matas, J., Panning, M., & Romanowicz, B. (2009). Measurement and implications of frequency dependence of attenuation. *Earth and Planetary Science Letters*, *282*(1–4), 285–293. https://doi.org/10.1016/j.epsl.2009.03.030
Maaløe, S. (2004). The solidus of harzburgite to 3 GPa pressure: The compositions of primary abyssal tholeiite. *Mineralogy and Petrology*, *81*(1–2), 1–17. https://doi.org/10.1007/s00710-004-0028-6
Molinari, I., & Morelli, A. (2011). EPcrust: A reference crustal model for the European plate. *Geophysical Journal International*, *185*(1), 352–364. https://doi.org/10.1111/j.1365-246X.2011.04940.x
Montelli, R., Nolet, G., Dahlen, F. A., Masters, G., Engdahl, E. R., & Hung, S. H. (2004). Finite-frequency tomography reveals a variety of plumes in the mantle. *Science*, *303*(5656), 338–343. https://doi.org/10.1126/science.1092485
Mosca, I., Cobden, L., Deuss, A., Ritsema, J., & Trampert, J. (2012). Seismic and mineralogical structures of the lower mantle from probabilistic tomography. *Journal of Geophysical Research*, *117*, B06304. https://doi.org/10.1029/2011JB008851
Mosegaard, K., & Tarantola, A. (1995). Monte-Carlo sampling of solutions to inverse problems. *Journal of Geophysical Research*, *100*(B7), 12,431–12,447. https://doi.org/10.1029/94JB03097

Olugboji, T. M., Karato, S., & Park, J. (2013). Structures of the oceanic lithosphere-asthenosphere boundary: Mineral-physics modeling and seismological signatures. *Geochemistry, Geophysics, Geosystems*, *14*, 880–901. https://doi.org/10.1002/ggge.20086

Priestley, K., & McKenzie, D. (2006). The thermal structure of the lithosphere from shear wave velocities. *Earth and Planetary Science Letters*, *244*, 285–301. https://doi.org/10.1016/j.epsl.2006.01.008

Resovsky, J., Trampert, J., & Van der Hilst, R. D. (2005). Error bars for the global seismic Q profile. *Earth and Planetary Science Letters*, *230*, 413–423. https://doi.org/10.1016/j.epsl.2004.12.008

Rickers, F., Fichtner, A., & Trampert, J. (2012). Imaging mantle plumes with instantaneous phase measurements of diffracted waves. *Geophysical Journal International*, *190*(1), 650–664. https://doi.org/10.1111/j.1365-246X.2012.05515.x

Romanowicz, B. (1994). Anelastic tomography: A new perspective on upper mantle thermal structure. *Earth and Planetary Science Letters*, *128*(3-4), 113–121. https://doi.org/10.1016/0012-821X(94)90139-2

Romanowicz, B., & Mitchell, B. J. (2007). 1.21—Deep Earth structureQ of the Earth from crust to core. In G. Schubert (Ed.), *Treatise on geophysics* (pp. 731–774). Amsterdam: Elsevier. https://doi.org/10.1016/B978-044452748-6.00024-9

Shito, A., Karato, S., Matsukage, K. N., & Nishihara, Y. (2006). Towards mapping the three-dimensional distribution of water in the upper mantle from velocity and attenuation tomography. In S. D. Jacobsen & S. van der Lee (Eds.), *Earth's deep water cycle* (pp. 225–236). Washington, DC: American Geophysical Union.

Simutė, S., Steptoe, H., Cobden, L., Gokhberg, A., & Fichtner, A. (2016). Full-waveform inversion of the Japanese islands region. *Journal of Geophysical Research: Solid Earth*, *121*, 3722–3741. https://doi.org/10.1002/2016JB012802

Stixrude, L., & Lithgow-Bertelloni, C. (2005). Thermodynamics of mantle minerals—I. Physical properties. *Geophysical Journal International*, *162*(2), 610–632. https://doi.org/10.1111/j.1365-246X.2005.02642.x

Stixrude, L., & Lithgow-Bertelloni, C. (2011). Thermodynamics of mantle minerals—II. Phase equilibria. *Geophysical Journal International*, *184*(3), 1180–1213. https://doi.org/10.1111/j.1365-246X.2010.04890.x

Tan, B., Jackson, I., & Gerald, J. F. (2001). High-temperature viscoelasticity of fine-grained polycrystalline olivine. *Physics and Chemistry of Minerals*, *28*(9), 641–664. https://doi.org/10.1007/s002690100189

Trampert, J., & Fichtner, A. (2013). Global imaging of the Earth's deep interior: Seismic constraints on (an) isotropy, density and attenuation. In *Physics and chemistry of the deep Earth* (pp. 324–350). Oxford: John Wiley & Sons, Ltd. https://doi.org/10.1002/9781118529492.ch11

Van der Hilst, R., Widiyantoro, S., & Engdahl, E. (1997). Evidence for deep mantle circulation from global tomography. *Nature*, *386*(6625), 578–584. https://doi.org/10.1038/386578a0

Wei, S. S., Wiens, D. A., Zha, Y., Plank, T., Webb, S. C., Blackman, D. K., et al. (2015). Seismic evidence of effects of water on melt transport in the lau back-arc mantle. *Nature*, *518*(7539), 395–398. https://doi.org/10.1038/nature14113

Yang, Y., Forsyth, D. W., & Weeraratne, D. S. (2007). Seismic attenuation near the east pacific rise and the origin of the low-velocity zone. *Earth and Planetary Science Letters*, *258*(1–2), 260–268. https://doi.org/10.1016/j.epsl.2007.03.040

Zerr, A., Diegeler, B., & Boehler, R. (1998). Solidus of the Earth's deep mantle. *Science*, *281*, 243–236.

Zhu, H., Bozdag, E., Duffy, T. S., & Tromp, J. (2013). Seismic attenuation beneath Europe and the North Atlantic: Implications for water in the mantle. *Earth and Planetary Science Letters*, *381*, 1–11. https://doi.org/10.1016/j.epsl.2013.08.030

Zhu, H., Bozdag, E., Peter, D., & Tromp, J. (2012). Structure of the European upper mantle revealed by adjoint tomography. *Nature Geoscience*, *5*(7), 493–498. https://doi.org/10.1038/ngeo1501

Zhu, H., Bozdag, E., & Tromp, J. (2015). Seismic structure of the European upper mantle based on adjoint tomography. *Geophysical Journal International*, *201*(1), 18–52. https://doi.org/10.1093/gji/ggu492